

Control Release of Adenosine Potentiate Osteogenic Differentiation within a Bone Integrative EGCG-g-NOCC/Collagen Composite Scaffold toward Guided Bone Regeneration in a Critical-Sized Calvarial Defect

Neeraj K. Verma, Aditya K. Kar, Amrita Singh, Pankaj Jagdale, Neeraj K. Satija, Debabrata Ghosh, and Satyakam Patnaik*



Cite This: *Biomacromolecules* 2021, 22, 3069–3083



Read Online

ACCESS |



Metrics & More

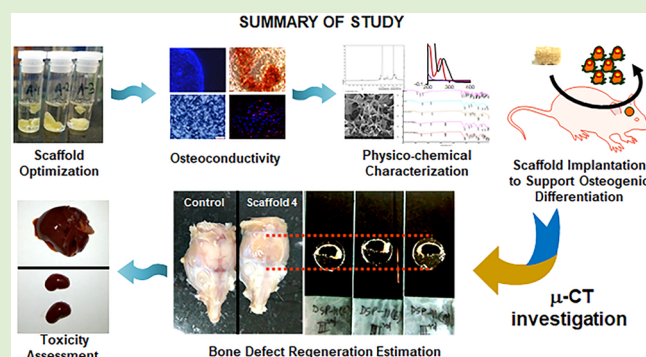


Article Recommendations



Supporting Information

ABSTRACT: The regeneration of critical-sized bone defects with biomimetic scaffolds remains clinically challenging due to avascular necrosis, chronic inflammation, and altered osteogenic activity. Two confounding mechanisms, efficacy manipulation, and temporal regulation dictate the scaffold's bone regenerative ability. Equally critical is the priming of the mesenchymal stromal cells (MSCs) toward lineage-specific differentiation into bone-forming osteoblast, which particularly depends on varied mechanochemical and biological cues during bone tissue regeneration. This study sought to design and develop an optimized osteogenic scaffold, adenosine/epigallocatechin gallate-*N,O*-carboxymethyl chitosan/collagen type I (AD/EGCG-g-NOCC@clgn I), having osteoinductive components toward swift bone regeneration in a calvarial defect BALB/c mice model. The *ex vivo* findings distinctly establish the pro-osteogenic potential of adenosine and EGCG, stimulating MSCs toward osteoblast differentiation with significantly increased expression of alkaline phosphatase, calcium deposits, and enhanced osteocalcin expression. Moreover, the 3D matrix recapitulates extracellular matrix (ECM) properties, provides a favorable microenvironment, structural support against mechanical stress, and acts as a reservoir for sustained release of osteoinductive molecules for cell differentiation, proliferation, and migration during matrix osteointegration observed. Evidence from *in vivo* experiments, micro-CT analyses, histology, and histomorphometry signify accelerated osteogenesis both qualitatively and quantitatively: effectual bone union with enhanced bone formation and new ossified tissue in 4 mm sized defects. Our results suggest that the optimized scaffold serves as an adjuvant to guide bone tissue regeneration in critical-sized calvarial defects with promising therapeutic efficacy.



INTRODUCTION

Bone healing is a complex and conserved cascade of molecular and cellular events.¹ Favorable spatiotemporal orchestration in the cellular pool near fractured bone site is crucial for rapid restoration of bone defects.² Advanced developments in material science have guided paradigm shifts in the innovations of bone tissue engineering to meet the present and future demands.^{3–7} In this context, regenerative scaffolds tailored to the bone defect microenvironment can play a crucial role in rapid bone tissue regeneration and remodeling by stimulating necessary biological cues. Currently, two strategies are clinically gaining attention in critical size bone injuries: one approach uses scaffolds having bioresponsive components, viz. osteoconductive and osteoinductive, to induce the endogenous cellular milieu comprising immune cells and stem/stromal progenitor cells to boost the healing and bone regeneration.¹ The other approach deals in *in situ* ectopic cellular

reprogramming via delivery of transcription and trophic factors, RNA-based therapeutics, epigenetic modulation through suitable biomaterials, and *in vivo* gene editing.⁸ These innovative therapeutic avenues require concerted efforts in developing efficacious scaffolds yielding excellent osteogenic and high osteoinductive attributes to succeed clinically. This approach is advantageous over existing autografts and allografts avoiding associated donor site morbidity. Moreover, a thorough understanding and screening of factors during the bone regeneration process will thus enable selection of suitable

Received: April 21, 2021

Revised: June 5, 2021

Published: June 21, 2021



bioresponsive materials (both natural and synthetic) that mimics the bone microenvironment at the fractured bone site with the possibility of sequential optimization process during scaffold preparation. This will ultimately facilitate healing, integration, and remodeling of the new bone formation by circumventing lower therapeutic index and side effects.⁹

Among the existing treatment modalities, therapeutic agents releasing osteogenic scaffolds could be the best alternative. Consequently, ideal scaffold candidates should be bioresponsive, without toxic implications, release the entrapped bioactive component(s) in a controlled and sustained manner, withstand mechano-physical stress/strain without compromising its structural integrity, and finally undergo biodegradability/resorbability to elicit a synergistic bone repair. Optimizing the scaffold design, structure, and surface attributes is therefore paramount for bone healing strategies.

Glycosaminoglycans, in particular chitosan, is a versatile cationic biopolymer possessing many properties such as antimicrobial, antioxidant, anticancer, and so on. Apart from resembling the extracellular matrix components, it is extensively used for a plethora of applications in the field of drug delivery as well as in bone graft substitutes (BGS).^{10–13} Carboxymethyl chitosan (CMC), a chitosan derivative, has been recently explored for its pro-osteogenic role^{14–16} and has better aqueous solubility and offers freedom of surface modifications through additional carboxylic groups compared to chitosan. Moreover, chitosan as a scaffolding material for bone tissue engineering, as a vehicle for growth factor delivery, and as an injectable gel for periodontal regeneration is well documented.^{17,18} Likewise, collagen, a major component of bone microarchitecture, plays a key role in maintaining bone homeostasis and force transmission.^{19–21} Type I collagen, a structural protein present in bone tissue, is known to be crucial in maintaining osteoblast phenotype and abundantly present in the extracellular matrix at the early and late stage of bone tissue regeneration and therefore being used extensively in bone regenerative scaffolds.^{22–24}

Recent studies emphasize the synergistic actions between BGS and several active biomolecules like growth factors, peptides, and small molecules toward rapid bone healing which are already in the commercial domain or in different phases of clinical trials.¹ One such molecule, adenosine triphosphate (ATP), and P2 purinergic signaling pathways have been specifically studied in detail for their role in bone metabolism.^{25–28} Interestingly, recent findings show adenosine to be a key signaling molecule that acts through purinergic receptors P1, although confronting results do exist.^{25,29,30} Moreover, it is not well understood how adenosine, a metabolite of ATP, locally and systemically influences the bone marrow derived mesenchymal cell populations toward osteogenesis in a bone defect. Although, it is known that origin-dependent traits of MSCs are altered by the tissue microenvironment. Recent understanding of adenosine's role in bone formation, resorption, and repair suggests adenosine signaling pathways to be a critical factor. Recently, Takedachi et al. showed the role of local and systemic adenosine in the modulation of antitumor responses *in vivo*. They have used CD73 null mice to unveil a potential role of adenosine in osteoblast differentiation.³¹ Carroll and colleagues have studied the role of the A2B AR in osteoblast differentiation and function by analyzing bone homeostasis *in vivo* using the A2B AR knockout (KO) mice model. They showed that at 9 and 12 days after osteoinduction fewer mineralized nodules were

found in bone marrow from A2B AR KO mice, suggesting a reduction in osteoblast differentiation in the absence of the A2B AR.³²

Epidemiological studies have correlated lower risk of hip fractures by observing a higher bone mineral density (BMD) in the habitual tea drinking population.³³ EGCG, one of the major constituents of various types of tea, is exhaustively reviewed for its role in bone homeostasis, in both cell-based and animal studies. Several plausible mechanisms have been proposed for its osteoprotective and osteogenic activity.^{34–36}

With the above facts in the backdrop, we aimed to develop a scaffold delivery system taking advantage of intrinsic osteogenic attributes of the above composite materials through a sequential optimization process toward rapid restoration of critical-sized bone defects. We hypothesize the optimization process adopted will overcome the shortfall of synthetic matrices by providing a multitude of osteogenic components in an optimum ratio to act cooperatively during bone healing. To the best of our knowledge, we have shown for the first time that the local delivery of adenosine and antioxidant EGCG together from the scaffold maintains a favorable microenvironment near the injured site to augment bone healing. As a proof of concept, bone tissue regeneration performance, biocompatibility, and the osteogenic potential of designed composite hydrogel scaffolds with optimized components were investigated by *in vitro*, *ex vivo*, and *in vivo* in calvarial bone defect of the BALB/c mice model utilizing μ CT as well as histomorphometry techniques.

■ MATERIALS AND METHODS

Materials. Medium molecular weight chitosan (degree of deacetylation 75–85%, MW 190–310 kDa), collagen type I solution from rat tail (#cat. no. C3867), (–)-epigallocatechin gallate (EGCG: #cat. no. E4143), adenosine (suitable for cell culture), 3-(4,5-dimethylthiazol-2-yl)-2,5-diphenyltetrazolium bromide (MTT), cetylpyridinium chloride (CPC), glutaraldehyde (GA) 25% water solution, α -minimum essential medium (α -MEM) suitable for cell culture, calcein, and the HT15 Trichrome Stain (Masson) Kit were purchased from Merck-Sigma (St. Louis, MO). Osteocalcin (OCN) antibody was from Santa Cruz Biotechnology (Santa Cruz, CA), BCIP (5-bromo-4-chloro-3-indolyl phosphate) (NBT, nitro blue tetrazolium) was from TCI Chemicals Pvt. Ltd. (India), alamarBlue cell viability reagent was from Invitrogen, Thermo Fisher Scientific (Waltham, MA), and trypsin-EDTA (0.25%) and fetal bovine serum (FBS) were from Gibco, Thermo Fisher Scientific (USA). All other reagents and solvents were of the highest purity and used as received. Milli-Q water (Millipore, Billerica, MA) was filtered with a 0.22 μ m syringe filter prior to use in all biochemical assays.

Ex Vivo Study. Bone Marrow Derived Mesenchymal Stromal Cells (BMSC) Isolation, Subculture, and Characterization. In this study, -8 to 10-week-old male BALB/c mice were housed for 12 h in light/dark conditions and fed ad libitum. Mice were anesthetized by using a cocktail of ketamine (25 mg/kg; Intas Pharma Ltd., Gujarat, India) and xylazine (2 mg/kg; Themis Medicare Ltd., Gujarat, India). The anesthetized mice' femur and tibia was isolated aseptically; epiphyses were excised to aspirate whole bone marrow, and BMSCs were isolated as described elsewhere.^{37,38} Postisolation, BMCs were transferred to α -MEM medium supplemented with 10% heat-inactivated FBS and antibiotics (100 units/mL penicillin G and 100 mg/mL streptomycin) (referred here onward as Growth Media A (GM-A)). MSCs were harvested and analyzed for expression of surface markers (fluorescence tagged anti-mouse antibodies Sca-1, CD11b; Miltenyi Biotech, CA) by a flow cytometer (BD influx v7 cell sorter, BD Biosciences, USA) using the standard protocol provided by the supplier. Data were analyzed on BD FACS software. Sixth to tenth passage cells were further used for experiments.

Cell Viability Assay. BMSCs were seeded into 96-well plates at a density of 3×10^3 cells/well. Cells were incubated with GM-A, and adenosine supplemented GM-A, for 7 days at 37 °C in a humidified incubator supplemented with 5% CO₂. The culture medium was replenished with fresh media every alternate day, and cell viability was determined by MTT using a microplate reader (FLUOstar Omega, BMG Labtech, Germany).³⁹ Cells were imaged by using an inverted microscope (Leica DMi1, Leica Microsystems, Wetzlar, Germany).

Alkaline Phosphatase (ALP) Staining. ALP staining was performed by using BCIP/NBT as reported previously.^{40,41} Briefly, on day 14, harvested cells were washed in PBS and fixed in 4% paraformaldehyde for 30 min prior to incubation in ALP buffer (pH 9.5, 5 min). Subsequently, ALP staining was done by incubating cells in a dye solution for 5 min followed by washing with PBS to remove the extra stain. Adequately stained fields of view were chosen and imaged under a Leica DMi1 inverted microscope (Leica Microsystems, Wetzlar, Germany). Likewise, ALP activity was performed for cells cultured in adenosine supplemented GM-A to judge its osteogenic potency. ImageJ software (National Institutes of Health, Bethesda, MD) was used to quantify areas of stained images.

Alizarin Red S Staining and Quantification for Matrix Mineralization. The extent of calcium deposition was determined by alizarin red S staining. On day 21, media was removed and cells were rinsed with PBS before being fixed with 70% ethanol for 10 min, washed again with PBS, and stained with 0.5% alizarin red S, pH 4.1, for 10 min at room temperature. Subsequently, cells were washed three times with Milli-Q water to remove the unincorporated dye. For quantification, cells were incubated with 10% cetylpyridinium chloride (CPC), and the OD measured at 550 nm by using a spectrophotometer. Similarly, the matrix mineralization assay was performed with BMSCs exposed to adenosine supplemented GM-A for evaluating the lineage-specific differentiation potential of extracellular adenosine. Stained images were obtained by a Leica inverted microscope.

Immunocytochemistry Assay. On day 21, culture media was discarded and cells were washed repeatedly with PBS and fixed in 4% formaldehyde at room temperature for 15 min. Subsequently, after washing, cells were kept in PBST blocking buffer (3% (w/v) BSA + 0.1% (v/v) Triton X-100 dissolved in PBS) for 60 min at room temperature. Fixed cells were incubated with a primary antibody, osteocalcin (1:100 dilution), for 16 h at 4 °C followed by washing with PBS and subsequently incubated under Alexa flour conjugated secondary anti-mouse antibody (1:250 dilution) at room temperature for 60 min. Finally, cell nuclei were stained with DAPI, washed, mounted on slides using antifade mounting media (Vectashield: h1000), and imaged under confocal microscopy (CLSM) in 20× magnification (LSM 880 with Airyscan Carl Zeiss, Jena, Germany).

Scaffold Components Optimization. Type I Collagen Concentration Optimization. A multicomponent scaffold needs to be optimized with respect to each of its components to elicit a synergistic action during tissue engineering without compromising its mechanical integrity and biocompatibility.⁴² Thus, each of the components used in the scaffold in our case was optimized sequentially to impart enhanced osteoinductive and osteoconductive properties to the scaffold. In the first instance, *N*,*O*-carboxymethyl chitosan (NOCC) was prepared as per our published literature.⁴³ Post-NOCC synthesis, the feed ratio of NOCC to Type I collagen was carefully chosen⁴² for three different formulations viz. NOCC@Clgn I (10:0.5, 10:1, and 10:2; w/v %) and cross-linked by utilizing glutaraldehyde coupling chemistry described elsewhere⁴⁴ with some modifications. Briefly, a known amount of NOCC was dissolved in 0.1 M acetic acid by stirring at 8000 rpm for 2 h to yield 1% (w/v) solution. Similarly, type I collagen was dissolved in 0.05 M acetic acid, homogenized, and maintained at 4 °C overnight to yield 1% (w/v) suspension. Before mixing, both the solutions were sonicated, followed by blending in the above-mentioned ratios. Thereafter, a total of 0.3% (w/v) glutaraldehyde solution added dropwise to the reaction mixture. The gelling time was monitored and optimized to 10 min, wherein the reaction solution turns viscous. Afterward, the mixture was washed repeatedly with deionized water to remove any

unreacted components. Subsequently, the mixture was casted into 48-well plates aseptically, frozen at −20 °C overnight onto absolute ethanol, and followed by freeze-drying for 3 days at −110 °C in lyophilizer (ScanVac CoolSafe, LaboGene, Denmark). The reaction mixture volume was optimized to obtained scaffolds of approximately 5 mm × 2 mm size (width × height).

BMSCs Homing in Scaffold for Viability and Proliferation. The aforementioned NOCC@Clgn I scaffolds were assessed for their cytocompatibility by cell proliferation assay. For this, all the three scaffold formulations were sterilized with ethanol and washed sequentially with PBS and Media A. Thereafter, the scaffolds were fixed onto 24-well culture plates with sterilized parafilm. BMSCs suspended in 0.5 mL of medium at a density of 1.5×10^5 cells were seeded per scaffold ($n = 3$) and left undisturbed for 2 h at 37 °C in a humidified incubator to achieve cell adhesion. Subsequently, the BMSC seeded scaffolds were supplemented with 2 mL of GM-A which was replenished in every alternate day. On day 3 and day 7, cell viability was determined by alamarBlue assay using the supplier's protocol. A known amount of alamarBlue was added in culture media (1/10th of culture volume) and incubated for 6 h, after which the fluorescence was measured at excitation–emission wavelengths, 570 nm–585 nm, in a microplate reader. Control samples were prepared similarly without BMSC seeding.

Scaffold Cell Culture and Imaging on SEM. BMSCs were inoculated onto scaffold as mentioned in the **Scaffold Components Optimization** section. Post 3 weeks of incubation, the medium was aspirated; scaffolds were washed twice in PBS and suspended in 2.5% glutaraldehyde solution overnight at 4 °C. Afterward, scaffolds were washed with 0.1% sodium cacodylate for 10 min followed by serial dehydration in 15%, 30%, 60%, and 90% acetone for 15 min each. Finally, scaffolds containing BMSCs were dehydrated in absolute acetone thrice and kept for CPD (critical point drying) to remove moisture absolutely. At this point, a chunk of two different types of scaffolds i.e., seeded and unseeded scaffolds, of the same formulations mounted on conductive aluminum pin stubs by using adhesive carbon discs on both sides. The samples were processed for coating with platinum by using a sputter coater SC7640 (Quorum Technologies Ltd., UK) that allowed a thickness range of 3–6 nm of the sputtered layer to be coated on the sample surface, followed by imaging under SEM (Quanta FEG 450, FEI, Netherland). In addition, Hoechst nuclear staining was performed with the final formulation to show the osteoconductive nature of the scaffold.

Optimization of Adenosine Entrapment, Loading, and Release Kinetics within NOCC@clgn I Scaffolds. A physical entrapment approach was adopted to obtain adenosine encapsulation and its release kinetics within the three developed scaffolds to choose the most advantageous formulation. The adenosine-entrapped scaffolds were prepared analogously to the procedure described in the **Scaffold Components Optimization** section; with the exception that adenosine (total adenosine concentration is 100 µg/mL/well in HEPES buffer) was added to the reaction mixture, mixed thoroughly before the addition of the cross-linking agent glutaraldehyde. The overall scaffold to adenosine ratio was kept at 8:2 (w/w %). The adenosine release profile from the different synthesized scaffolds was performed by transferring the particular scaffold in a screw cap glass vial containing 10 mL of PBS placed on a temperature-controlled shaker maintained at 37 °C. To quantify adenosine release, 1 mL of suspended media aspirated for analysis and replenished with fresh media. The amount of adenosine released was calculated by using a standard calibration curve (conc vs abs; $\lambda_{\max} = 270$ nm) of adenosine. The encapsulation efficiency (% EE) and loading efficiency (% LE) were calculated by using the following formulas:

$$\% \text{ LE} = \frac{\text{weight of adenosine in scaffold}}{\text{weight of scaffold}} \times 100 \quad (1)$$

$$\% \text{ EE} = \frac{\text{amount of adenosine present in scaffold}}{\text{amount of adenosine used}} \times 100 \quad (2)$$

EGCG Grafting on NOCC. EGCG grafted NOCC (EGCG-g-NOCC) was prepared by using previously reported methodology with

modification.⁴⁵ Briefly, filtered aqueous NOCC solution (0.2 g) adjusted to pH 3.5 with 1 M hydrochloric acid (HCl) followed by addition of 0.5 mL of 1 M hydrogen peroxide (H₂O₂) containing 0.025 g of ascorbic acid. The reaction mixture was preheated to 40 °C for 1 h, 0.175 g (30 mM) of EGCG was added, and the mixture was left to stir overnight at 40 °C. To remove free EGCG, the total reaction mixture was dialyzed against Milli-Q in dialysis tubing (cutoff size 12 kDa, Sigma) for 2 days in the dark with intermittent water change and finally lyophilized to obtain EGCG grafted NOCC. The method was chosen due to its mild reaction condition requirement and nongeneration of toxic byproducts. NMR, FTIR, UV, and TGA techniques characterized EGCG-g-NOCC.

Final Scaffold Fabrication with Optimized Components (AD/EGCG-g-NOCC@clgn I). Based on the outcome of the optimization process, the final scaffold formulation (AD/EGCG-g-NOCC@clgn I) was synthesized with chosen EGCG-g-NOCC to collagen I ratio as 10:2 to elicit a desired synergistic action following the experimental procedure described in the **Scaffold Components Optimization** section with the exception that, in place of NOCC, EGCG-g-NOCC was used. Here onward the scaffolds are designated by 1 for NOCC, 2 for NOCC@clgn I, 3 for EGCG-g-NOCC@clgn I, and 4 for AD/EGCG-g-NOCC@clgn I.

Characterization of Scaffold Formulations. FTIR, NMR, and UV were used to confirm the successful synthesis of different formulations of scaffolds. The swelling ratio, TGA, and porosity were assessed to understand the hydrogel property and microarchitecture of scaffolds. All parameters examined by using standard procedures.

NMR. To check the successful synthesis, intermolecular interaction between functional groups of all used components of the scaffold was examined by ¹H NMR. The spectra of scaffolds were recorded on a Bruker Avance 400 MHz instrument (Bruker, Germany) by using appropriate solvents, and the chemical shifts are denoted in ppm.

FT-IR. The spectra of scaffolds 1, 2, 3, and 4 were recorded on an ATR-FT-IR spectrophotometer (Nicolet iSS, Thermo Scientific) for the range 4000–500 cm⁻¹ with 16 scans and a resolution of 4 cm⁻¹.

UV-Vis Analysis. To ascertain EGCG grafting onto NOCC, pure EGCG (0.3 mg/mL), NOCC (10 mg/mL), and EGCG-g-NOCC (10 mg/mL) solutions were analyzed by using a double-beam UV-vis spectrophotometer (lambda Bio 35, PerkinElmer, USA). An acetic acid–water solution (0.4%; v/v) was used as the blank solution.

Thermogravimetric Analysis (TGA). A thermogravimetric analyzer (TGA/DSC 3+ Mettler Toledo, Switzerland) determined the thermal stability of the scaffolds. Around 10–15 mg of the scaffold was used, and thermal stability was measured at a heating rate of 50 °C/min under a nitrogen atmosphere at a temperature ranging from 25 to 800 °C.

Porosity. The liquid displacement method was utilized to access the porosity of different scaffold formulations.⁴⁶ Briefly, the samples were immersed in absolute ethanol until saturation. The sample weights before and after immersion were used to get the porosity (%) by eq 3

$$\text{porosity (\%)} = \frac{W_{t_1} - W_{t_2}}{\rho V_1} \times 100 \quad (3)$$

where W_{t_1} and W_{t_2} are weights before immersion and after immersion in alcohol, respectively. V_1 is the volume of alcohol before immersion, and ρ is a constant (density of alcohol). The pore size analysis was done by using ImageJ software.

Swelling Ratio. To check the swelling, the dry weight of different formulations of scaffolds was recorded, and then each scaffold was immersed separately in PBS at room temperature to fully saturate overnight. Thereafter, scaffolds were swiftly placed on Whatman filter paper to remove surface moisture, and wet weight was recorded. The swelling ratio of scaffolds was determined via eq 4⁴⁷

$$\text{swelling ratio (\%)} = \frac{W_s - W_d}{W_d} \times 100 \quad (4)$$

where W_d is the dry weight of the scaffold and W_s is the wet weight of a fully saturated scaffold in PBS.

Subcutaneous Biocompatibility. The final optimized scaffold 4 was subcutaneously implanted by using a standard surgical procedure. Briefly, healthy male BALB/c mice ($n = 5$) were anesthetized by using a ketamine and xylazine cocktail. Dorsal hairs were shaved, cleaned, and sterilized followed by creating 7–8 mm subcutaneous pockets with a scalpel blade. The 5 mm sized scaffold 4 was implanted aseptically, and the incised area was sutured. After surgery, animals were kept under observation for 28 days in optimum conditions and sacrificed after 28 days for histopathological analysis.

In Vivo Study. Surgical Procedure for Calvarial Defect and μ -CT. All animal studies conducted were in accordance with protocols and guidelines approved by the Institutional Animal Ethics Committee of CSIR- Indian Institute of Toxicology Research (54/GORBi/S/CPCSEA, dated 28.03.2017, ref No. IITR/IAEC/52/17 and CSIR-IITR: 54/GO/RReRcBiBt/S/99/CPCSEA dated 22.02.2019). The guidelines are approved by the Committee for the Purpose of Control and Supervision of Experiments on Animals (CPCSEA), Ministry of Fisheries, Animal Husbandry & Dairying, Department of Animal Husbandry and Dairying, Government of India. Experiments were performed in triplicates until otherwise stated. All animals were housed under controlled conditions on a 12 h light/dark cycle and acclimatized for a week before the start of experiments. In this study, 9 week old healthy male BALB/c mice with 30 ± 4 g body weight were used. Calvarial defects were made according to previously reported literature.⁴⁸ Briefly, mice were anesthetized, and a midline incision was made on the skin covering the skull; both the skin and periosteum were retracted to reveal the cranium. Exactly 4 mm calvarial defects (4 mm in diameter, full thickness) were made in between the parietal bones with a sagittal suture line by using a 4 mm trephine bur attached to a dental handpiece with micromotor. To avoid heat-induced necrosis, all defects were made under constant saline irrigation. The mice were randomly divided into five groups ($n = 10$ /group) as follows: group 1: SHAM (calvarial bone defect mice without scaffold implant); group 2: NOCC scaffold implanted mice; group 3: NOCC@clgn I scaffolds implanted mice; group 4: EGCG-g-NOCC@clgn I scaffolds implanted mice; group 5: AD/EGCG-g-NOCC@clgn I scaffolds implanted mice. The prepared scaffolds of 5 mm diameter were placed above the area of the defect of the animals in all the groups except group 1: SHAM. To ensure the position of the scaffold confined only to the defect area, all scaffold formulations were fixed by using Amcrylate, Bio-Adhesive (Concord Drugs Limited, Hyderabad, Telangana, India). The periosteum was closed over the defects and sutured with absorbable 2-Vicryl sutures with Trugut Chromic Catgut USP 4-0. The stitched area was cleaned with povidone–iodine. Mice were monitored postsurgery for signs of distress, movement, and weight loss. Scaffolds were left in the calvarial defects for 2, 4, and 8 weeks following which mice were euthanized by injecting an overdose of ketamine intraperitoneally. The whole skull of mice was excised, cleaned, and placed in 10% neutral buffered formalin. The excised skulls were analyzed by using a high-resolution micro-CT system (Sky Scan 1076 μ CT scanner; SkyScan, Ltd., Kartuizersweg, Kontich, Belgium). Scans were performed at X-ray source 70 kVp and 142 mA with a pixel size of 9 μ m capturing images after every 0.8 rotation. Images were taken throughout 180° being averaged at each point. NRecon, DataViewer, and CTAn software were used for cross-sectional reconstruction in the region of interest (ROI), the volume of interest (VOI) for bone microarchitectural parameters analysis, and 3D images.⁴⁹

Histological and Histomorphometric Examination of Bone Repairment. Calcein labeling was performed for dynamic histomorphometric measures to estimate the levels of newly formed bone according to methods previously described.^{50,51} Briefly, calcein was administered (20 mg/kg, i.p.) 24 h before scarifies at 2, 4, and 8 weeks. Dyes were prepared freshly with 2% sodium bicarbonate, adjusted to pH 7.4, and filtered through a 0.45 μ m filter before being administered to the animals. Animals were euthanized, and whole skulls were retrieved and transferred into 10% saline-buffered formalin. Excised skulls were then embedded in polymerizing acrylic material (Orthoplast, India). The next day, 50 μ m bone cross sections

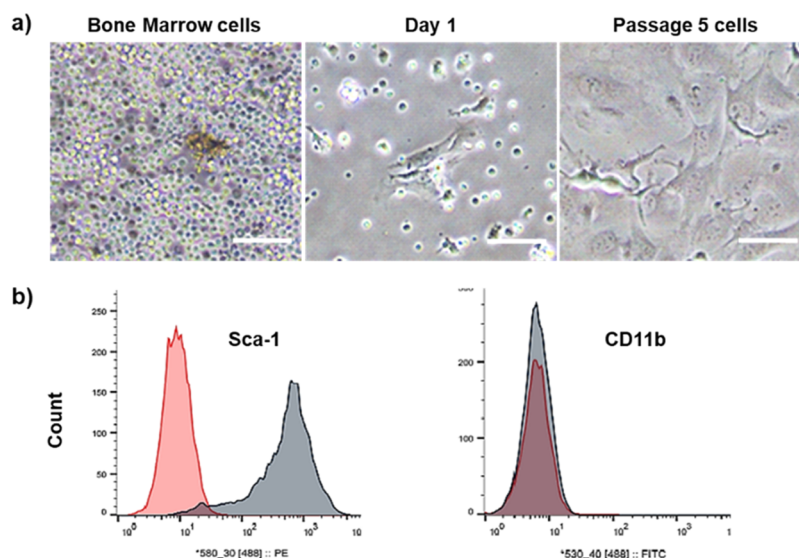


Figure 1. BMSCs isolation and characterization. (a) Representative phase-contrast morphological images of BMSCs. (b) Characterizations of BMSCs through cell markers (*Sca-1* and *CD11b*) expression by FACS of cells at the fifth passage. Data were acquired by using BD influx v7 cell sorter and analyzed on BD FACS software. Red is isotype control, and black is marker expression. All scale bars are 100 μm .

passing from the middle of the calvarial defect were made by using an IsoMet low-speed precision cutter (Buehler, USA). Bone sections were imaged by using CLSM and LSM 880 with Airyscan (Carl Zeiss, Jena, Germany) in 20 \times magnification.

Skull bones were decalcified by incubating in an aqueous solution of 0.5 M EDTA and 0.4 M sodium hydroxide at pH 7.0 until soft and pliable. The decalcified samples were dehydrated in ascending grades of alcohol up to 100% and were then embedded in paraffin wax blocks for sectioning. Paraffinized blocks were trimmed up to obtained desired defect area only and sectioned with a microtome (Leica RM2155; Leica Microsystems, Wetzlar, Germany) equipped with a tungsten carbide knife. Approximately three sections of each sample of 5 μm passing through the middle of the calvarial bone defects including other soft tissue were prepared and stained with H&E to observe the cytoplasm of osteoblasts and new bone formation under light microscopy (BX53Olympus, Japan). Masson's trichrome staining was performed as described by the manufacturer's instructions (HT15 Trichrome Stain (Masson) Kit; Sigma-Aldrich) to assess collagen and osteoid formation. Likewise, H&E staining was performed to check liver and kidney histopathology in scaffold-implanted mice. For quantitative analysis, Masson's trichrome staining images (2 \times) were used to measure newly formed bone area including edges and middle of the defect area, and data were reconfirmed with hematoxylin and eosin staining images (4 \times) passing through the same area. ImageJ 1.64 r software (National Institutes of Health, Bethesda, MD) was used to measure new bone formation by using three images from each sample. The percentage of new bone formation was calculated via eq 5:

$$\text{new bone (\%)} = \frac{\text{newly formed bone area}}{\text{total calvarial bone defect area}} \times 100 \quad (5)$$

Hematological and Biochemical Analyses. Collected blood samples from all the groups were analyzed for complete blood count as well as liver and kidney functions to assess any toxicological implication of the scaffold. Various biochemical parameters, namely, white blood cells (WBC), red blood cells (RBC), hemoglobin (HGB), hematocrit (HCT), mean corpuscular volume (MCV), mean corpuscular hemoglobin (MCH), mean cell hemoglobin concentration (MCHC), platelets (PLT), red cell distribution width (RDW-SD and RDW-CV), platelet distribution width (PDW), mean platelet volume (MPV), platelet larger cell ratio (P-LCR), plateletcrit (PCT), neutrophils, lymphocytes, monocytes, eosinophils, and basophils, were analyzed by using an automated hematology analyzer (Sysmex-1800i, Japan). For biochemical analysis, the collected blood samples

were allowed to clot in a stagnant position for 1 h at room temperature and then centrifuged at 4000 rpm for 10 min at 4 $^{\circ}\text{C}$ in a refrigerated centrifuge (Sigma, USA). Serum supernatant was aspirated and analyzed for biochemical parameters, namely glucose, creatinine, urea, aspartate aminotransferase (AST), cholesterol, and alanine aminotransferase (ALT) by using an automated clinical chemistry analyzer (Rx Daytona, Randox, UK). Before analysis, the instrument was calibrated with analytes by using calibrator and control sera.

Statistical Analysis. Experiments were performed in at least triplicate, and results were expressed as mean \pm standard deviation (SD). Statistical analysis was performed by using GraphPad Prism software, version 5.03 (Graph Pad software, La Jolla, CA). The difference between the two groups was analyzed by a two-tailed Student's test, and data between three or more groups were analyzed by one-way ANOVA with Tukey post-test for multiple comparisons. Differences of $P < 0.05$ (*), $P < 0.01$ (**), and $P < 0.001$ (***) were considered statistically significant.

RESULTS

Ex Vivo Studies. BMSCs Isolation and Characterization.

Bone residing MSCs are the precursor of the osteoblast during new bone formation. Therefore, MSCs were isolated from whole bone marrow culture from male BALB/c mice as described previously⁵² and characterized for their purity and stemness. Figure 1a shows phase contrast images of freshly isolated BMSCs at day 1, passage mix culture with floating hematopoietic population, and BMSCs at passage 5. BMSCs were characterized by flow cytometry, and $\sim 95\%$ of the cells were found positive for stem cell marker *Sca-1* devoid of macrophage as $< 5\%$ were found positive for *CD11b* marker shown in Figure 1b. These characterized MSCs were used in further *ex vivo* studies.

BMSCs Viability upon Exposure to Adenosine. Figure S1a reveals there was hardly any impact on the population of the BMSCs evidenced from microscopic observations of the cultured cells. Initially, BMSCs viability upon exposure to adenosine was performed in a concentration-dependent manner (0–200 $\mu\text{g}/\text{mL}$), and the MTT assay suggested that adenosine has hardly any effect on their viability up to day 7 as shown in Figure S1b. Based on the outcome from the viability

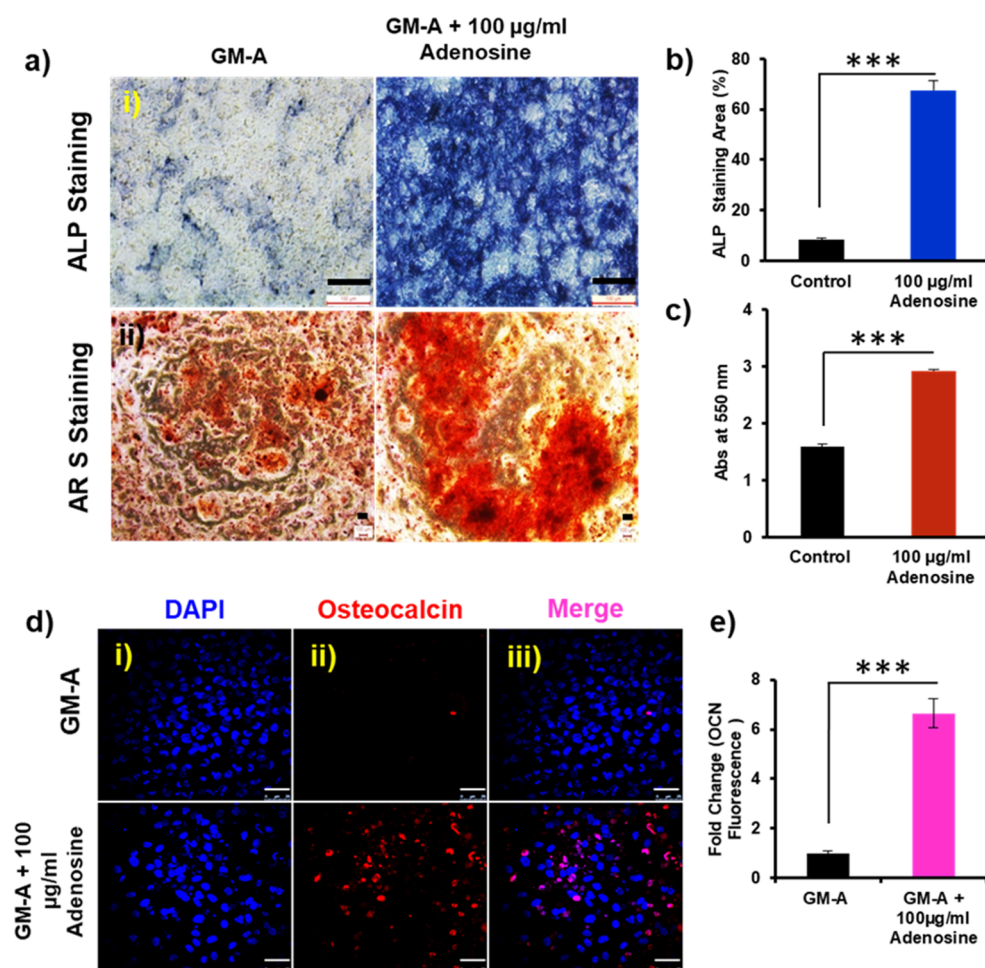


Figure 2. Pro-osteogenic activity of adenosine. (a) Compared representative images of (i) ALP activity at day 14 and (ii) matrix mineralization (Alizarin S staining) assay at day 21 between cells cultured with growth medium A and adenosine-supplemented growth medium A (GM-A). The scale bar is 100 µm in the respective compared group. Quantitative measurement of (b) ALP activity at day 14 and (c) matrix mineralization at day 21. (d) Representative ICC Images showing the immuno-staining of osteocalcin: a known osteoblast marker at day 21. Scale bar is 25 µm. (e) Osteocalcin estimation by ImageJ software from NIH, Bethesda, MD ($n = 3$). Error bars represent mean \pm standard error. GM-A = growth media A (α -MEM medium supplemented with 10% heat-inactivated FBS and antibiotics). Statistical significance $P < 0.05$ (*), $P < 0.01$ (**), and $P < 0.0001$ (***) is relative to control.

assay, a 100 µg/mL concentration of adenosine was selected for subsequent studies.

Adenosine Induces Pro-Osteogenic Differentiation in BMSCs. To determine pro-osteogenic activity, all experiments were performed at 100 µg/mL adenosine concentration. Following confirmatory results from viability experiments, we then checked to establish the role of adenosine as an osteogenic agent in mesenchymal differentiation. Toward this, ALP, a marker of differentiated osteoblast was checked by BCIP/NBT staining at day 14.⁴¹ As shown in the middle panel of Figure 2a(i), higher ALP activity was observed in BMSCs incubated in adenosine supplemented GM-A medium compared to only GM-A medium. Figure S1c shows representative microscopic images for the same.

Figure 2a(ii), lower panel, depicts an intensified alizarin red S staining in BMSCs incubated with adenosine supplemented GM-A compared to control. Figure 2b shows a more than 6-fold increase in the quantitative expression of ALP compared to control. Matrix mineralization was found to be (1.84 ± 0.04) -fold more in adenosine supplemented BMSCs compared to control at day 21 and shown in Figure 2c. The final stage of osteogenesis was examined by immunocytochemistry (ICC)

on day 21. Figure 2d shows ICC images for the expression of osteocalcin (OCN), a late osteoblast marker, which was observed to be significantly higher in BMSCs, incubated with adenosine supplemented GM-A compared to control. The quantitative expression of ICC is shown in Figure 2e. The fold change in fluorescence of OCN in immuno-stained images was estimated by using ImageJ software and found to around 6-fold compared to control ($2.01 \pm 1.01\%$ and $12.09 \pm 3.6\%$ for control and GM-A with adenosine, respectively) at day 21.

Scaffolds Preparation and Characterization. NOCC Synthesis, Type I Collagen Concentration Optimization, and EGCG Grafting on NOCC. NOCC was synthesized and characterized by using NMR, FT-IR, and UV spectroscopies. Moreover, as shown in Figure S2a, the chemical shift at 3.0 ppm was assigned to C2 proton while the broad chemical shifts for glucosamine residues of NOCC were observed for the $-\text{CH}_2-\text{COO}^-$ at C2 (N-position) and at C6 (O-position) protons at 4.4 and 4.6 ppm, which are in agreement with the literature. In addition, the peak at 3.22 was assigned as the $-\text{NHCO}$ proton while the multiplet peaks observed between 3.4 and 3.8 correspond to C3–C6 protons of the pyranose ring. The methyl protons of the *N*-acetylglucosamine residues

appear at 1.9 ppm. These observations denote successful carboxylation of chitosan and agree with the published literature.^{53,54} For the EGCG@NOCC in Figure S2a, additional signals were visible in the region between 2.5 and 3.0 ppm, suggesting EGCG grafting. Moreover, because of the low degree of substitution, there are no observable peaks in the aromatic region of the spectra. EGCG moieties may be embedded deep within the polymeric core that restricts the exposure of the aromatic protons.⁵⁵ In addition, extra peaks were observed between 1.83 and 1.89, which are assigned to the methyl proton, while the aromatic residues (between 8.0 and 8.6 ppm) and amide residues signals (between 9.5 and 10 ppm) were also observed in the spectra of EGCG-g-NOCC@clgn I. More so, the peak seen at 3.9 ppm in Figure S2c corresponds to the proton on the hydroxylated carbon of hydroxyproline of collagen.⁵⁶

Figure S2d depicts UV spectra of NOCC which had no absorption band in between 200 and 400 nm. However, for the spectrum of EGCG, the λ_{\max} was observed at 273 nm, arising due to the $\pi-\pi^*$ transition of the aromatic group which has a red-shift to 260 nm in the EGCG grafted NOCC. This indicates EGCG moieties were successfully conjugated to the NOCC albeit a low degree of substitution, $\sim 2.4\%$, was observed. The feed ratio between NOCC to type I collagen was optimized for scaffold synthesis to improve the osteoconductivity and adenosine release profile. Moreover, collagen concentration plays a crucial role in eliciting favorable biological, mechanical, and structural attributes necessary for successful bone tissue engineering.^{42,57}

For this, NOCC and type I collagen were blended in 10:0.5, 10:1, and 10:2 (w/v %) ratios with 0.3% (w/v) glutaraldehyde cross-linking to form three different NOCC@clgn I scaffolds. Figure 3a (upper panel) shows SEM images of the three formulations without any gross differences in cross-linked patterns. It was observed that a more uniform pore size was successively achieved by increasing the type I collagen concentration. To affirm the cell viability and proliferation in scaffolds, MSCs were seeded with the same number of cells and observed by alamarBlue assay at days 3 and 7 which is shown in Figure 3c. We observed both 10:1 and 10:2 formulations showed (2.95 ± 0.40) - and (3.32 ± 0.19) -fold increase in cell viability, respectively, compared to 10:0.5 formulation at day 7. However, the cell proliferation ability in all the three individual NOCC/type I collagen formulations was observed to be more or less similar $(5.07 \pm 0.93, 6.99 \pm 1.39, \text{ and } 6.17 \pm 0.27)$ for 10:0.5, 10:1, and 10:2 formulations, respectively from day 3 to 7 (Figure 3c).

Similar observations were witnessed in the SEM analyses of the MSCs seeded scaffolds (Figure 3a, lower panel). The above preliminary finding suggested a significant impact of the increasing type I collagen concentration on the proliferation of BMSCs and led us to opt for 10:2 as our chosen formulation for further optimizations. Hoechst staining was performed to assess the biocompatibility of the developed scaffolds (10:2), and as observed from Figure 3b(ii,iii) the scaffold exhibits excellent biocompatibility offering a 3D environment for the cells to proliferate and migrate compared to the cells cultured without scaffold.

Adenosine Entrapment, Release Kinetics, and Osteogenic Potential within the Scaffold. Once the active composition was decided, adenosine was entrapped within different formulations to assess its osteoinductive potential. It is now well established that spatiotemporal release of active

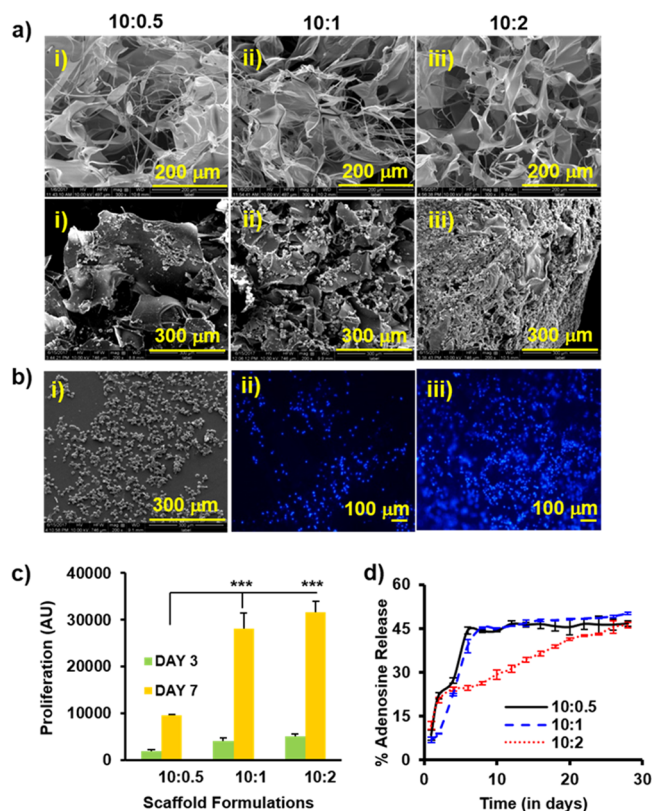


Figure 3. Representative SEM and microscopy images of different formulations of NOCC@clgn I scaffolds and their cytocompatibility. (a, upper panel, i–iii) SEM images showing the scaffolds exhibiting a high degree of interconnectivity with porous networks for the feed ratio of NOCC to type I collagen as (i) 10:0.5, (ii) 10:1, and (iii) 10:2. Scale bar is 200 μm (upper panel). (a, lower panel, i–iii) SEM images of cell-seeded scaffolds of 10:0.5, 10:1, and 10:2 formulations at 3 weeks. Scale bar is 300 μm (lower panel). (b, i) SEM images of MSCs cells. (b, ii) Representative microscopic images of Hoechst stained MSCs without scaffold and (b, iii) MSCs cultured within NOCC@clgn I scaffold (10:2). Scale bar is 100 μm for the microscopic images and 300 μm for SEM. (c) Cell proliferation assay within scaffolds using a hemocytometer, where an equal number of MSCs were seeded followed by cell density quantification by alamarBlue on day 3 and 7. (d) Adenosine release kinetics from the different NOCC@clgn I scaffolds suggesting the 10:2 formulation ratio offers a sustained release of the entrapped adenosine over 30 days ($n = 3$). $P < 0.001$ (***) is relative to 10:0.5 formulation. Error bars represent mean \pm standard error.

components from a regenerative matrix at any kind of injury site is essential toward a rapid healing process. Therefore, the release kinetics of adenosine was monitored in the developed scaffolds. Figure 3d shows the release profile of adenosine from the three formulations. The result suggested an ideal slow and sustained pattern of release was exhibited by NOCC to type I collagen (10:2) scaffold formulation.

Characterization of Final Scaffold EGCG-g-NOCC@clgn I Formulation and Its Cytocompatibility. Following successful synthesis and physicochemical characterization (discussed in the NOCC Synthesis section) of NOCC and EGCG-g-NOCC, four different scaffold compositions, 1, 2, 3, and 4 (1 as NOCC, 2 as NOCC@clgn I, 3 as EGCG-g-NOCC@clgn I, and 4 as AD/EGCG-g-NOCC@clgn I), were formulated to evaluate their osteogenic potential in an *in vivo* setting on a mouse calvarial defect model. Figure 4a shows the

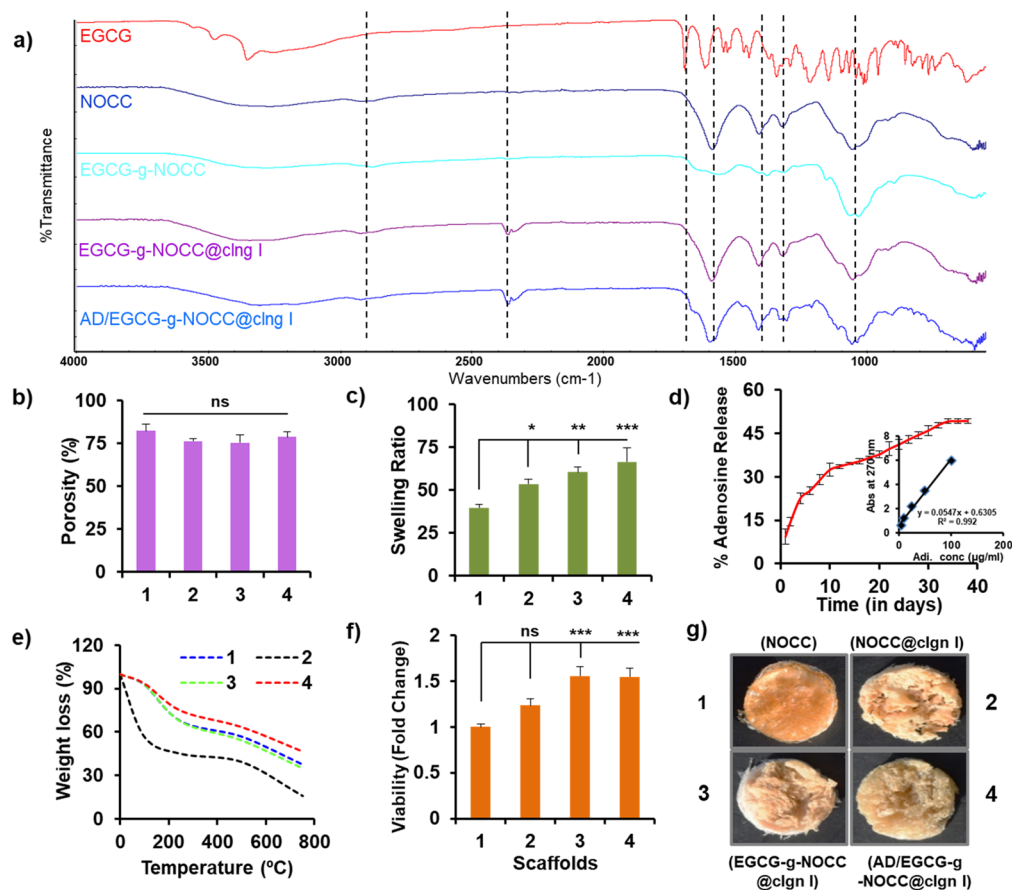


Figure 4. Physicochemical characterization of optimized scaffold formulation. (a) FT-IR spectra of NOCC, EGCG, EGCG-g-NOCC, and EGCG-g-NOCC@c1ng I scaffolds showing the sequential modifications. (b) Unaltered porosity of the final optimized scaffold formulation compared to its precursors suggests the sequential modifications does not affect the overall porosity in the final formulation even after adenosine entrapment. (c) Overnight swelling behavior of scaffolds suggests the final formulation, 4, offers maximum swelling of the scaffold, which in turn helps in proliferation and migration of the MSCs leading to a higher lineage-specific differentiation potential. (d) Entrapped adenosine release kinetics from the AD/EGCG-g-NOCC@c1ng I scaffold highlighting the sustained release potential of the matrix over 5 weeks. Inset: adenosine calibration curve used to quantify cumulative release at 270 nm. (e) TGA spectra of the scaffolds show AD/EGCG-g-NOCC@c1ng I have the best stability profile compared to other formulations. (f) MSCs viability in different scaffolds suggests a 1.5-fold increase in the viability in optimized scaffold 4 compared to the 1 in a 7-day culture. (g) Pictures of different scaffolds postsynthesis. Error bars represent mean \pm standard error. $n = 3$ /group. 1: NOCC; 2: NOCC@c1ng I; 3: EGCG-g-NOCC@c1ng I; 4: AD/EGCG-g-NOCC@c1ng I. Statistical significance $P < 0.05$ (*), $P < 0.01$ (**), and $P < 0.001$ (***) is relative to 1.

combined FT-IR spectra of all scaffold formulations to identify the functional groups and their interaction. Post EGCG grafting onto NOCC, the characteristic peaks of pyranose structure at 1154 and 1080 cm^{-1} had a red-shift in 1. Moreover, the strong absorption bands at 1584 and 1408 cm^{-1} assigned to amide bands I and II, respectively, in NOCC were broadened in scaffold 2 due to the aromaticity of the EGCG. In addition, the sharp 1690 cm^{-1} peak of EGCG is broadened in the spectrum of scaffold 2, indicating that the hydroxyl radical catalyzed the grafting of EGCG onto NOCC. Subsequently, the appearance of additional peaks between 2500 and 2000 cm^{-1} in scaffold 3 corroborated the presence of type I collagen.⁵⁸ The above observations point toward a successful synthesis of all scaffold formulations. The porosity of all scaffold formulations is shown in Figure 4b, revealing the percent porosity of 1, 2, 3, and 4 scaffolds to be 82.14 ± 3.8 , 76.10 ± 1.65 , 75.27 ± 4.58 , and 78.69 ± 2.98 , respectively. The result demonstrated subsequent modification, and entrapment of adenosine had no significant impact on the overall porosity, albeit offering a high 3D porous network within the scaffold conducive for proliferation and migration of cells.

Figure 4c shows the swelling ratio of all scaffold formulations. Interestingly, there is an increasing trend in swelling efficiency observed across the scaffolds with 4 displaying maximum swellability of $66.59 \pm 7.95\%$ followed by 3, 2, and 1 with $60.55 \pm 2.76\%$, $53.49 \pm 2.80\%$, and $39.70 \pm 1.87\%$, respectively. This suggested that the sequential addition of osteogenic components has a positive impact on swelling behavior of the final scaffold formulation.

We then evaluated the release profile of adenosine entrapped within 4, and as expected, a similar trend was observed akin to the 10:2 (NOCC@c1ng I) formulation confirmed in Figure 4d. The percent entrapment and loading efficiency of adenosine were found to be $39.77 \pm 2.01\%$ and $7.95 \pm 0.40\%$, respectively. Figure 4e shows the thermal stability of all scaffold formulations by TGA. As evidenced, the percent weight loss of 1, 2, 3, and 4 were $\sim 59\%$, 80% , 60% , and 48% , respectively, suggesting that heat-induced weight loss was minimum in 4, which in turn suggests its ample mechanical rigidity and thermal stability compared to rest of scaffold formulations.

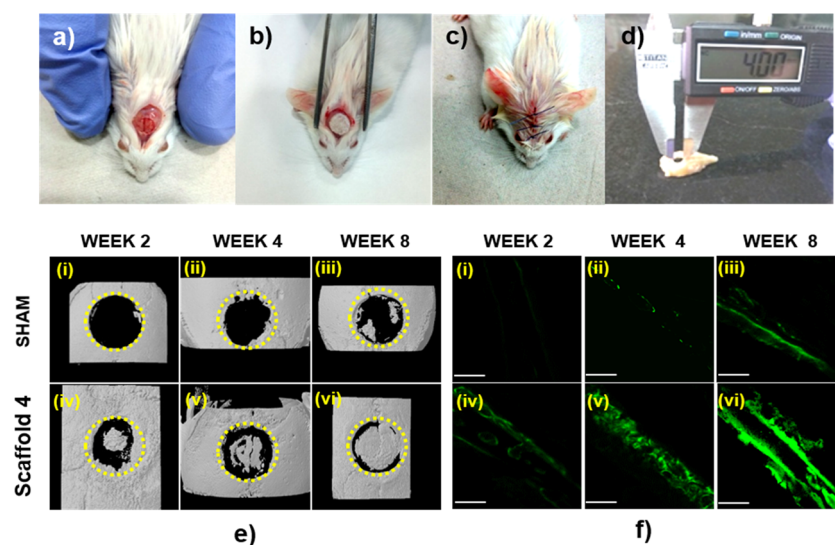


Figure 5. Representative images of surgical procedure adopted for 4 mm sized calvarial defect in BALB/c mice model. (a) SHAM control without any scaffold implant showing calvarial defect created with a trephine burr. (b) Scaffold 4 (AD/EGCG-g-NOCC@cln I) implantation over the defect. (c) Scaffold implanted mice showing sutured skin at the defect site. (d) A 4 mm sized defect on the excised skull of a mice measured by a Vernier caliper. (e) μ -CT 3D reconstruction images of calvarial defect at selected time points (2, 4, and 8 weeks) of SHAM control and scaffold 4. (f) Confocal fluorescence microscopy images of calcein labeling in middle of the defect showing new bone growth in (i–iii) control group and (iv–vi) scaffold 4 at selected time points (2, 4, and 8 weeks). The scale bar is 200 μ m. The dotted line highlights the defect area.

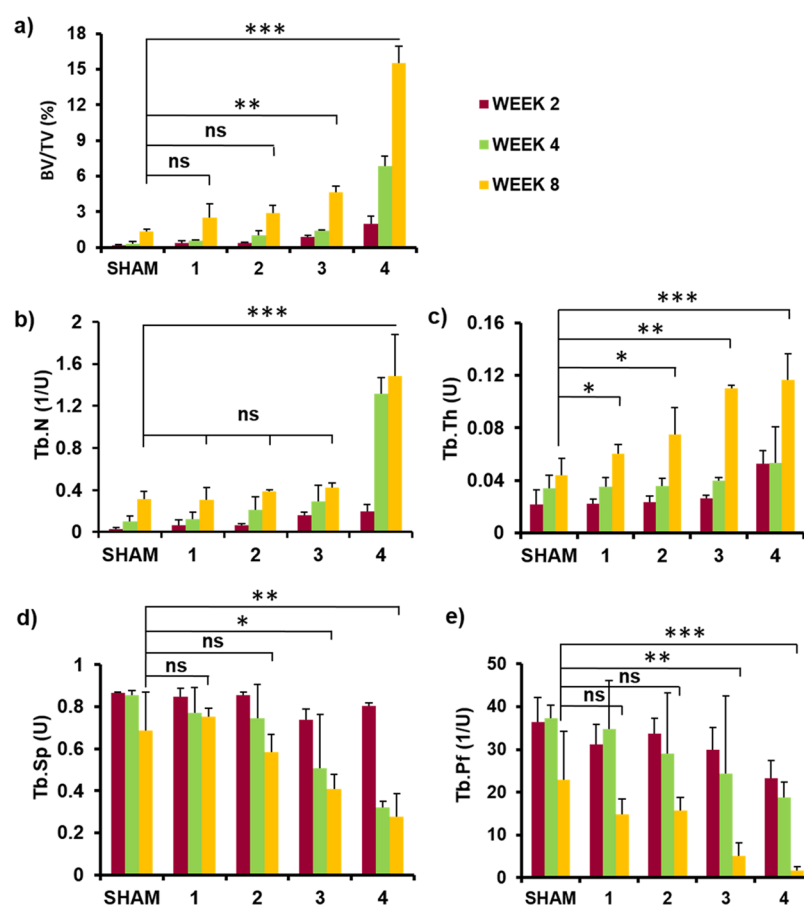


Figure 6. Quantitative assessment of bone morphometric parameters with different scaffolds obtained at calvarial defect area at week 8. Microarchitectural parameters of newly formed bone tissue: (a) Percentage of quantified bone tissue volume (BV/TV) compared to SHAM control. (b) Trabecular number (Tb.N). (c) Trabecular thickness (Tb.Th). (d) Trabecular separation (Tb.Sp). (e) Trabecular pattern factor (Tb.Pf). 1: NOCC; 2: NOCC@cln I; 3: EGCG-g-NOCC@cln I; 4: AD/EGCG-g-NOCC@cln I. Statistical significance $P < 0.05$ (*), $P < 0.01$ (**), and $P < 0.001$ (***) is relative to SHAM (without scaffold implant). Error bars represent mean \pm standard error.

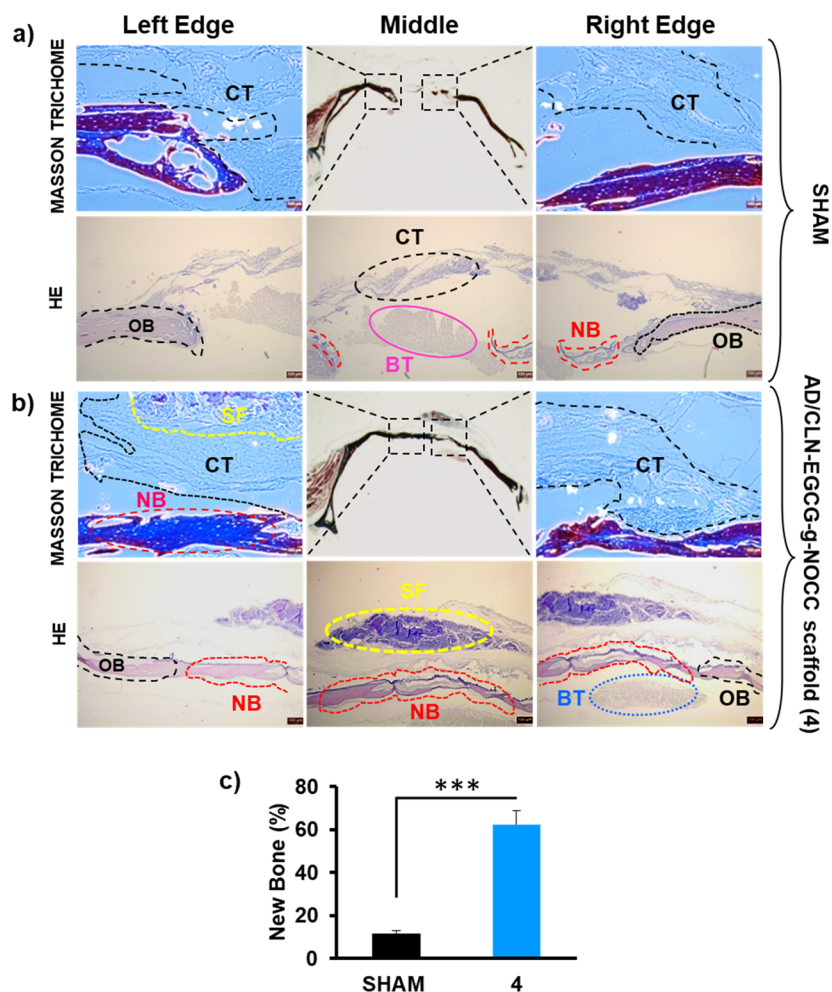


Figure 7. : Representative histomorphometry analysis of critical-sized calvarial defect: Masson's trichrome staining and HE staining at week 8 postsurgery. (a) SHAM control (without scaffold). (b) Scaffold 4 (AD/EGCG-g-NOCC@clng I). The upper middle panel in both the groups is stereoscope images showing the coronal section of critical-sized calvarial bone defect at low magnification, 4 \times . (c) Quantification of new bone formation within defect area at week 8 of the surgery. Scale bar is 100 μ m in both MT and HE staining. CT: connective tissue; BT: brain tissue; OB: old bone; NB: new bone; SF: scaffold. Statistical significance $P < 0.001$ (***) is relative to SHAM control. Error bars represent mean \pm standard error.

Finally, to check the osteogenic potential of all the active components, BMSCs were seeded within the four developed scaffolds and evaluated for their ability to elicit any synergistic action for cell proliferation and migration within the scaffold's architecture. Figure 4f shows the cell viability in 1, 2, 3, and 4 on day 7. Scaffolds 3 and 4 showed more or less similar viability of MSCs which is $\sim 1.54 \pm 0.09$ times higher compared to 1, suggesting that the final scaffold 4 offers a conducive environment for the cells to proliferate and migrate within the scaffold architecture. The representative physical appearance of scaffolds 1, 2, 3, and 4 is shown in Figure 4g. Once the final optimized scaffold formulation, 4, was synthesized and successfully characterized eliciting all the favorable attributes, we then check its *in vivo* biocompatibility by subcutaneous implantation of the scaffold 4 on the dorsal side of BALB/c mice as shown in Figure S3a. As anticipated, we did not observe any toxicity of scaffold 4, evidence from the normal tissue architectures, and the histological analysis of skin sections shown in Figure S3b,c.

AD/EGCG-g-NOCC@clng I Induced Bone Regeneration in Critical-Sized Calvarial Defects. *In Vivo* Reconstruction of Calvarial Defects. The efficacy of AD/EGCG-g-

NOCC@clng I scaffold to promote bone regeneration postsurgical procedure in a critical-sized calvarial defect in adult mice was assessed and analyzed. Figure 5a–d shows the representative snapshots of the adopted surgical procedure and the 4 mm sized critical calvarial defect. Figure 5e exhibits the 3D reconstruction images of critical-sized calvarial defects of BALB/c mice generated by μ CT analysis of different groups. At 2 weeks, all scaffold formulations implanted mice showed the appearance of new bone tissue and initiation of mineralization except the control group shown in Figure 5e–i. While new bone formation was observed starting from the edge to the middle of the defect area in all the groups, it was more pronounced in animal groups implanted with scaffold 3 in Figure S4a(iii) and scaffold 4 in Figure 5(e–iv) at 2 weeks of postimplantation. As compared to SHAM control, bone mineralization was consistently accelerated at week 4 and 8, and as anticipated, scaffold 4 showed the maximum amount of mineralized new bone tissues in the defect region at week 8. We then performed calcein labeling to access the extent of mineralization in the newly formed bone in the defect area. Figure 5f shows the fluorescence images of calcein labeling in the midsection of calvarial defects of groups implanted with

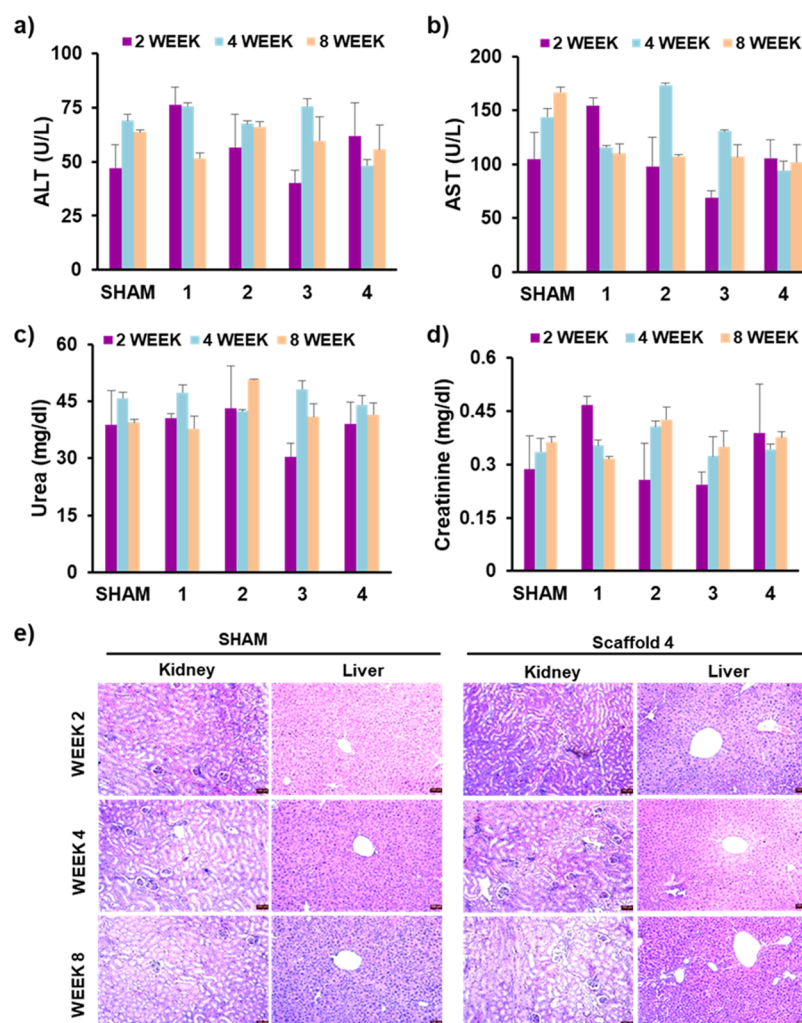


Figure 8. Biochemical parameters and H&E staining. The biochemical parameters such as (a) ALT, (b) AST, (c) urea, and (d) creatinine levels across all the groups show no significant change confirming the biocompatible nature of the scaffolds ($n = 5$). Similarly, the histochemical analysis of (e) liver and kidney function display no apparent alteration in the group implanted with scaffold 4 compared to the SHAM control. The scale bar is 100 μm . ($n = 3$). Error bars represent mean \pm standard error.

scaffold 4 and SHAM control for the 2, 4, and 8 weeks time interval. The results are consistent with the μCT data, and as depicted in Figure S4f(vi) and Figure S4b(iii), the scaffold 4 implanted mice group showed higher fluorescence intensity, indicating the maximum matrix mineralization compare to other groups at week 8 of postimplantation.

As shown in Figure 6a–c, a comparison between all animal groups was made to differentiate the bone-forming ability of different scaffold formulations at week 8. A higher difference was observed for BV/TV %, Tb.N, and Tb.Th between SHAM control and mice implanted with scaffold 4.

However, Tb.Sp and Tb.Pf showed a decreasing trend shown in Figure 6d,e. These observations of critical parameters for bone regeneration suggest that scaffold 4 has the superior ability to induce osteogenesis by enhancing bone formation with a faster and better bone integration within a critical-sized calvarial defect, postimplantation at week 8.

Histological Study. Masson's Trichrome staining and H&E staining were performed to compare the osteogenesis in the SHAM control group and scaffold 4 implanted group as histological evidence to further support the μCT findings. Figure 7 shows the representative histological cross sections images of Masson's Trichrome stained bone tissues. The

presence of newly formed fibrous connective tissues was observed in both groups at week 8 depicted in Figure 7a,b (upper panel). However, as shown in Figure 7b (upper panel), higher collagen deposition was observed in the defect area of scaffold 4 implanted group at week 8 compared to SHAM control (without scaffold), although a considerable amount of woven bone with osteoid formation was seen in both the groups at the edges of the defect at week 2 and 4 postimplantation (data not shown). However, the midsection of the defect was gradually filled by lamellar bone only in scaffold 4 implanted group at week 8 of postimplantation, suggesting the osteogenic potential of scaffold 4. Additionally, H&E staining was performed to examine newly formed tissues in the defect site. Osteoblast cells were seen with collagen fiber deposition and mineralization in both groups. Nonetheless, in the scaffold 4 implanted group, a more pronounced new bone tissue formation was seen in the calvarial defect region compared to SHAM control as shown in Figure 7a,b (lower panels). Taken together, a substantial amount of cellular infiltration was observed in the scaffold 4 group revealing active participation of the scaffold materials to achieve the maximum new bone formation in the bone defect area. A significant increase in new bone formation in terms of bone

percentage was also observed from the semiquantitative analysis⁵⁹ and depicted in Figure 7c.

Hematology and Biochemistry Parameters. Hematological parameters were analyzed to examine the toxicological consequences in scaffold implanted animal groups and are shown in Figure 8a–d.

Hematological analysis reveals the biocompatible and nontoxic nature of all formulations, wherein ALT, AST, creatinine, and urea level are observed to be in the normal range as per CPCSEA guidelines, suggesting liver and kidney functioned normally throughout the study period. In addition, H&E staining of the liver and kidney sections revealed no apparent alteration in the tissue microstructures at weeks 2, 4, and 8 presented in Figure 8e. Additionally, bodyweight measurement for the selected time duration of the study (Figure S5) and detailed hematological values at necropsy (Table S1) revealed no abnormalities, and the values are within the in normal range, suggesting the superior biointegration and biocompatibility of our designed scaffold.

DISCUSSION

MSCs are the precursors for bone-forming osteoblast during bone defect restoration. Therefore, we decided to use BALB/c's bone marrow derived MSCs to gauge the osteogenic potential of our designed scaffolds *ex vivo* before utilizing them in *in vivo* conditions. We aimed to assess the biocompatibility, osteoconductivity, and osteoinductivity of our scaffold. To begin with, four pro-osteogenic bioinspired components, namely adenosine, *N,O*-carboxymethyl chitosan, collagen type I, and EGCG, were chosen to prepare the scaffolds.

Recently, adenosine's role in bone metabolism and homeostasis gained a deeper understanding.^{25–27,29} When adenosine is supplemented extracellularly, purinergic receptors mediate its physiological and pharmacological activity through G-protein coupled receptors. These receptors are recently identified as modulators of osteoblast/osteoclast differentiation, their functions, and overall bone homeostasis.^{28,60} Before using in *in vivo* conditions, the role of adenosine was established as a potential pro-osteogenic agent for bone marrow derived MSCs *ex vivo*. Adenosine was found cytocompatible with BMSCs for up to 7 days.

Alkaline phosphatase (ALP) is a well-known early marker of osteogenesis, and its high activity is very crucial during the initial phase of osteogenic differentiation.⁶¹ In our case, the high activity of ALP was identified on day 14. In addition, OCN, another marker expressed on the mature osteoblast, was enhanced significantly at day 21. Taking together these observations, we could establish that adenosine induces and promotes pro-osteogenic differentiation of bone marrow derived MSCs into the osteoblast.

Critical-sized bone defect healing often requires either an osteogenic environment or osteoinductive growth factors around the injury site to have a successful cell-based bone regeneration and repair process. Epidemiological studies revealed a positive correlation between habitual tea drinkers and a lower risk of hip fractures in postmenopausal women of several countries.⁶² The role of EGCG, one of the green tea catechins,⁶³ in this context has been probed to establish its association with bone metabolism. Apart from its diverse roles as anticancer, antioxidant, anti-inflammatory, antiatherogenic, and so on, it was shown to have lineage-specific pro-osteogenic differentiation in hBMSCs^{35,62} and human adipose-derived stem cells (hASCs).³⁴

Considering all the above cues, we designed our composite scaffold for guided bone regeneration driven by spatiotemporal delivery of adenosine together with EGCG, NOCC, and type I collagen as an osteogenic supporting matrix. We observed the tailored scaffold could distinctly induce lineage-specific differentiation in the BMSCs precursor cells toward osteoblast. We confirmed our hypothesis by assessing and analyzing various osteogenic parameters both in *in vitro* and *in vivo* scenarios using critical-sized bone defects in a BAB/c mouse model. In any soft matter implant, scaffolding materials are very crucial for augmenting cell adhesion and proliferation resulting in successful osteointegration in bone tissue engineering.⁶⁴ It is already established that (i) glucosamines (chitosan/hyaluronic acid/chondroitin sulfate/heparin, etc.) and its derivatives are excellent scaffolding material for their osteoconductive and osteoinductive nature⁶⁵ and (ii) type I collagen enhances the cellular adhesion and osteoblast differentiation.^{66,67} Moreover, there are several reports where various formulations of chitosan or its derivatives and type I collagen have been used as composite/hybrid/hydrogels for bone tissue engineering.^{13,68,69} Taking together these facts, we chose NOCC with the added advantage of postmodification at its substituted carboxyl group terminal and conjugated EGCG, a multifunctional bioactive molecule. EGCG was incorporated in our scaffolds to influence the inflammatory response during the bone healing process.³³ Studies have reported that EGCG promotes pro-osteogenic differentiation apart from its well-known anti-inflammatory propensity.^{34,35,70,71}

In addition, we optimized EGCG modified NOCC's ratio with type I collagen concentration using glutaraldehyde cross-linking to design our scaffolds. A 10:2 feed ratio EGCG-g-NOCC and type I collagen were finally chosen based on successful physicochemical characterizations for subsequent *in vitro* and *in vivo* evaluation. The *ex vivo* studies on day 21 revealed improved cell adhesion and proliferation of the BMSCs due to collagen content of the scaffold.⁷² Nonetheless, the cross-linking process enhanced the surface area offering porous networks within the 3D matrix. Additionally, the optimized scaffolding network showed a controlled release of entrapped adenosine in a prolonged and sustained fashion, which in turn induces osteogenic differentiation. In total, four scaffolds were fabricated in a sequentially optimized process to assess optimal therapeutic efficacy.

Spectroscopic data suggested the successful synthesis of all scaffold formulations with desired properties. Physical factor like porosity plays an important role in nutrient diffusion and cell migration during osteogenesis.^{73,74} Swelling behavior is also very crucial for cellular infiltration. Porosity, thermal stability, swelling behavior, and cell viability characteristic of the scaffolds collectively establish scaffolds 3 and 4 are adequate for the implant.

Finally, all four formulations were evaluated for their *in vivo* efficacy in a critical-sized calvarial defect in BALB/c mice. Although, all scaffolds display osteoinductive characteristics, yet the final formulation, scaffold 4, distinctly showed a better bone healing performance observed from the μ -CT and histopathology analysis. A higher bone tissue formation was noticed in the calvarial defect region in the animal group implanted with scaffold 4 due to the presence of adenosine showing pro-osteogenic activity through its controlled and sustained release at the wound site. Moreover, hematology and biochemistry parameters indicated a nontoxic nature of our scaffolds. Anticipating the bone-forming ability, our final

optimized scaffold 4 showed maximum therapeutic effect just because a multitude of all osteogenic components is available in optimum ratio to act cooperatively. As far as the individual component is considered, deliberate release of adenosine in a sustained manner might attract more BMSCs at the defect site, NOCC, and type I collagen may integrate with the defect site to increase the early and late markers of osteogenesis, EGCG, to regulate the bone metabolism to favor osteogenesis.

CONCLUSION

The current study demonstrates a unique bone tissue-engineering strategy to design and develop biomimetic hydrogel scaffolds for successful bone defect repair and restoration process. *Ex vivo* studies established the potential role of adenosine on BALB/c mice-derived BMSCs in guiding lineage-specific differentiation into the osteoblast. In addition, component optimization of the hydrogel scaffold results in a highly porous network structure. This ensures a high degree of swellability of the matrix for homing BMSCs, inducing pro-osteogenic differentiation into bone-forming osteoblast, and cell proliferation by providing a favorable milieu for bone repair and regeneration process. Finally, *in vivo* assessment confirmed the optimized scaffold 4 was suitable for regeneration and repairment of a critical-sized calvarial defect in the BALB/c mice model. This strategy could offer an effective biomimetic bone replacement platform attuned to a specific bone microenvironment for the construction of a scaffold that recapitulates the unique cellular, structural, and functional properties of the native bone.

ASSOCIATED CONTENT

Supporting Information

The Supporting Information is available free of charge at <https://pubs.acs.org/doi/10.1021/acs.biomac.1c00513>.

- (1) Adenosine impact on BMSCs, (2) physicochemical characterization of different scaffolds during the optimization process, (3) representative images of *in vivo* biocompatibility assessment of final scaffold 4 (AD/EGCG-NOCC@clgn I) formulation at 8 weeks, (4) representative images of critical-sized bone defect in BALB/c mice, and (5) bodyweight of experimental animals of different groups at 2, 4, and 8 weeks postsurgery; (6) tables showing hematology parameters (PDF)

AUTHOR INFORMATION

Corresponding Author

Satyakam Patnaik – Water Analysis Laboratory, Nanomaterial Toxicology Group, CSIR-Indian Institute of Toxicology Research (CSIR-IITR), Lucknow, Uttar Pradesh 226001, India; Academy of Scientific and Innovative Research (AcSIR), Ghaziabad 201002, India; orcid.org/0000-0003-4920-236X; Phone: (+91)-522-2627586; Email: satyakampatnaik@iitr.res.in, satyakampatnaik@yahoo.com; Fax: (+91)-522-2628227

Authors

Neeraj K. Verma – Water Analysis Laboratory, Nanomaterial Toxicology Group, CSIR-Indian Institute of Toxicology Research (CSIR-IITR), Lucknow, Uttar Pradesh 226001, India; College of Dental Sciences, BBD University, Lucknow, Uttar Pradesh 226028, India

Aditya K. Kar – Water Analysis Laboratory, Nanomaterial Toxicology Group, CSIR-Indian Institute of Toxicology Research (CSIR-IITR), Lucknow, Uttar Pradesh 226001, India; Academy of Scientific and Innovative Research (AcSIR), Ghaziabad 201002, India

Amrita Singh – Water Analysis Laboratory, Nanomaterial Toxicology Group, CSIR-Indian Institute of Toxicology Research (CSIR-IITR), Lucknow, Uttar Pradesh 226001, India; Academy of Scientific and Innovative Research (AcSIR), Ghaziabad 201002, India

Pankaj Jagdale – Regulatory Toxicology Group, CSIR-Indian Institute of Toxicology Research (CSIR-IITR), Lucknow, Uttar Pradesh 226001, India

Neeraj K. Satija – Academy of Scientific and Innovative Research (AcSIR), Ghaziabad 201002, India; Developmental Toxicology Laboratory, Systems Toxicology & Health Risk Assessment Group, CSIR-Indian Institute of Toxicology Research (CSIR-IITR), Lucknow, Uttar Pradesh 226001, India

Debabrata Ghosh – Immunotoxicology laboratory, Food Drug and Chemical Toxicology Group, CSIR-Indian Institute of Toxicology Research (CSIR-IITR), Lucknow, Uttar Pradesh 226001, India; Academy of Scientific and Innovative Research (AcSIR), Ghaziabad 201002, India

Complete contact information is available at: <https://pubs.acs.org/10.1021/acs.biomac.1c00513>

Author Contributions

S.P., N.K.V., and D.G. ideated the concept designed experiments, interpreted data, and wrote the manuscript. N.K.V., A.K.K., and A.S. performed the experimental work. P.J. helped in surgical procedures and histopathology studies. N.S. helped in *ex vivo* studies.

Notes

The authors declare no competing financial interest. The CSIR-IITR manuscript communication number is 3689. Data will be made available on request.

ACKNOWLEDGMENTS

Partial financial support for this work from CSIR, India, project (NanoSHE), and DBT (GAP-368 and) is gratefully acknowledged. N.K.V. was supported by Project NanoSHE/FTT-MLP-008, A.K.K. was supported by UGC-SRF fellowship, and A.S. was supported by ICMR-SRF fellowship. We acknowledge Dr. P. N. Saxena for SEM analysis and Mrs. N. Arjaria for confocal imaging. The authors also greatly acknowledge Dr. Naibedya Chattopadhyay, Chief Scientist, Division of Endocrinology, CSIR-CDRI, and Dr. Shailendra Maurya, CSIR-CDRI, for helping to conduct micro-CT examination and their valuable inputs.

REFERENCES

- (1) Ho-Shui-Ling, A.; Bolander, J.; Rustom, L. E.; Johnson, A. W.; Luyten, F. P.; Picart, C. Bone regeneration strategies: Engineered scaffolds, bioactive molecules and stem cells current stage and future perspectives. *Biomaterials* **2018**, *180*, 143–162.
- (2) Perez, R. A.; Seo, S.-J.; Won, J.-E.; Lee, E.-J.; Jang, J.-H.; Knowles, J. C.; Kim, H.-W. Therapeutically relevant aspects in bone repair and regeneration. *Mater. Today* **2015**, *18* (10), 573–589.
- (3) Koons, G. L.; Diba, M.; Mikos, A. G. Materials design for bone-tissue engineering. *Nat. Rev. Mater.* **2020**, *5* (8), 584–603.
- (4) Harvestine, J. N.; Gonzalez-Fernandez, T.; Sebastian, A.; Hum, N. R.; Genetos, D. C.; Loots, G. G.; Leach, J. K. Osteogenic

preconditioning in perfusion bioreactors improves vascularization and bone formation by human bone marrow aspirates. *Sci. Adv.* **2020**, *6* (7), eaay2387.

(5) Henkel, J.; Woodruff, M. A.; Epari, D. R.; Steck, R.; Glatt, V.; Dickinson, I. C.; Choong, P. F. M.; Schuetz, M. A.; Huttmacher, D. W. Bone Regeneration Based on Tissue Engineering Conceptions - A 21st Century Perspective. *Bone Res.* **2013**, *1* (1), 216–248.

(6) Zhang, K.; Wang, S.; Zhou, C.; Cheng, L.; Gao, X.; Xie, X.; Sun, J.; Wang, H.; Weir, M. D.; Reynolds, M. A.; et al. Advanced smart biomaterials and constructs for hard tissue engineering and regeneration. *Bone Res.* **2018**, *6* (1), 31.

(7) Hasan, A.; Byambaa, B.; Morshed, M.; Cheikh, M. I.; Shakoob, R. A.; Mustafy, T.; Marei, H. E. Advances in osteobiologic materials for bone substitutes. *J. Tissue Eng. Regen. Med.* **2018**, *12* (6), 1448–1468.

(8) Gaharwar, A. K.; Singh, I.; Khademhosseini, A. Engineered biomaterials for in situ tissue regeneration. *Nat. Rev. Mater.* **2020**, *5* (9), 686–705.

(9) Khosla, S. Increasing options for the treatment of osteoporosis. *N. Engl. J. Med.* **2009**, *361* (8), 818–20.

(10) Di Martino, A.; Sittinger, M.; Risbud, M. V. Chitosan: a versatile biopolymer for orthopaedic tissue-engineering. *Biomaterials* **2005**, *26* (30), 5983–5990.

(11) Kim, I.-Y.; Seo, S.-J.; Moon, H.-S.; Yoo, M.-K.; Park, I.-Y.; Kim, B.-C.; Cho, C.-S. Chitosan and its derivatives for tissue engineering applications. *Biotechnol. Adv.* **2008**, *26* (1), 1–21.

(12) Dong, L.; Wang, S.-J.; Zhao, X.-R.; Zhu, Y.-F.; Yu, J.-K. 3D-printed poly (ϵ -caprolactone) scaffold integrated with cell-laden chitosan hydrogels for bone tissue engineering. *Sci. Rep.* **2017**, *7* (1), 13412.

(13) Levengood, S. L.; Zhang, M. Chitosan-based scaffolds for bone tissue engineering. *J. Mater. Chem. B* **2014**, *2* (21), 3161–3184.

(14) Yu, Z.; Xiao, C.; Huang, Y.; Chen, M.; Wei, W.; Yang, X.; Zhou, H.; Bi, X.; Lu, L.; Ruan, J.; Fan, X. Enhanced bioactivity and osteoinductivity of carboxymethyl chitosan/nanohydroxyapatite /graphene oxide nanocomposites. *RSC Adv.* **2018**, *8* (32), 17860–17877.

(15) Tao, L.; Zhonglong, L.; Ming, X.; Zeheng, Y.; Zhiyuan, L.; Xiaojun, Z.; Jinwu, W. In vitro and in vivo studies of a gelatin/carboxymethyl chitosan/LAPONITE® composite scaffold for bone tissue engineering. *RSC Adv.* **2017**, *7* (85), 54100–54110.

(16) Lu, Y.; Li, L.; Zhu, Y.; Wang, X.; Li, M.; Lin, Z.; Hu, X.; Zhang, Y.; Yin, Q.; Xia, H.; Mao, C. Multifunctional copper-containing carboxymethyl chitosan/alginate scaffolds for eradicating clinical bacterial infection and promoting bone formation. *ACS Appl. Mater. Interfaces* **2018**, *10* (1), 127–138.

(17) Saravanan, S.; Leena, R. S.; Selvamurugan, N. Chitosan based biocomposite scaffolds for bone tissue engineering. *Int. J. Biol. Macromol.* **2016**, *93*, 1354–1365.

(18) Venkatesan, J.; Anil, S.; Kim, S. K.; Shim, M. S. Chitosan as a vehicle for growth factor delivery: Various preparations and their applications in bone tissue regeneration. *Int. J. Biol. Macromol.* **2017**, *104*, 1383–1397.

(19) Tzaphlidou, M. Bone architecture: collagen structure and calcium/phosphorus maps. *J. Biol. Phys.* **2008**, *34* (1–2), 39–49.

(20) Viguier-Carrin, S.; Garnero, P.; Delmas, P. D. The role of collagen in bone strength. *Osteoporosis Int.* **2006**, *17* (3), 319–36.

(21) Dong, C.; Lv, Y. Application of Collagen Scaffold in Tissue Engineering: Recent Advances and New Perspectives. *Polymers* **2016**, *8* (2), 42.

(22) Nakashima, K.; de Crombrughe, B. Transcriptional mechanisms in osteoblast differentiation and bone formation. *Trends Genet.* **2003**, *19* (8), 458–466.

(23) Shi, S.; Kirk, M.; Kahn, A. J. The role of type I collagen in the regulation of the osteoblast phenotype. *J. Bone Miner. Res.* **1996**, *11* (8), 1139–1145.

(24) Chen, Y.; Chen, S.; Kawazoe, N.; Chen, G. Promoted Angiogenesis and Osteogenesis by Dexamethasone-loaded Calcium Phosphate Nanoparticles/Collagen Composite Scaffolds with Microgroove Networks. *Sci. Rep.* **2018**, *8* (1), 14143.

(25) Evans, B.; Ham, J. An emerging role for adenosine and its receptors in bone homeostasis. *Front. Endocrinol.* **2012**, *3*, 113.

(26) Mediero, A.; Kara, F. M.; Wilder, T.; Cronstein, B. N. Adenosine A2A receptor ligation inhibits osteoclast formation. *Am. J. Pathol.* **2012**, *180* (2), 775–786.

(27) Mediero, A.; Cronstein, B. N. Adenosine and bone metabolism. *Trends Endocrinol. Metab.* **2013**, *24* (6), 290–300.

(28) Evans, B. A. J. Does adenosine play a role in bone formation, resorption and repair? *Purinergic Signalling* **2012**, *8* (2), 177–180.

(29) Katebi, M.; Soleimani, M.; Cronstein, B. N. Adenosine A2A receptors play an active role in mouse bone marrow-derived mesenchymal stem cell development. *J. Leukocyte Biol.* **2009**, *85* (3), 438–444.

(30) Zurovec, M.; Dolezal, T.; Gazi, M.; Pavlova, E.; Bryant, P. J. Adenosine deaminase-related growth factors stimulate cell proliferation in *Drosophila* by depleting extracellular adenosine. *Proc. Natl. Acad. Sci. U. S. A.* **2002**, *99* (7), 4403–4408.

(31) Takedachi, M.; Oohara, H.; Smith, B. J.; Iyama, M.; Kobashi, M.; Maeda, K.; Long, C. L.; Humphrey, M. B.; Stoeker, B. J.; Toyosawa, S.; Thompson, L. F.; Murakami, S. CD73-generated adenosine promotes osteoblast differentiation. *J. Cell. Physiol.* **2012**, *227* (6), 2622–2631.

(32) Carroll, S. H.; Wigner, N. A.; Kulkarni, N.; Johnston-Cox, H.; Gerstenfeld, L. C.; Ravid, K. A2B adenosine receptor promotes mesenchymal stem cell differentiation to osteoblasts and bone formation in vivo. *J. Biol. Chem.* **2012**, *287* (19), 15718–27.

(33) Shen, C.-L.; Yeh, J. K.; Cao, J. J.; Wang, J.-S. Green tea and bone metabolism. *Nutr. Res. (N. Y., NY, U. S.)* **2009**, *29* (7), 437–456.

(34) Lin, S.-Y.; Kang, L.; Wang, C.-Z.; Huang, H.; Cheng, T.-L.; Huang, H.-T.; Lee, M.-J.; Lin, Y.-S.; Ho, M.-L.; Wang, G.-J.; Chen, C.-H. (–)-Epigallocatechin-3-Gallate (EGCG) Enhances Osteogenic Differentiation of Human Bone Marrow Mesenchymal Stem Cells. *Molecules* **2018**, *23* (12), 3221.

(35) Jin, P.; Wu, H.; Xu, G.; Zheng, L.; Zhao, J. Epigallocatechin-3-gallate (EGCG) as a pro-osteogenic agent to enhance osteogenic differentiation of mesenchymal stem cells from human bone marrow: an in vitro study. *Cell Tissue Res.* **2014**, *356* (2), 381–390.

(36) Daglia, M. Polyphenols as antimicrobial agents. *Curr. Opin. Biotechnol.* **2012**, *23* (2), 174–181.

(37) Kim, K. S.; Lee, J. Y.; Kang, Y. M.; Kim, E. S.; Kim, G. H.; Rhee, S. D.; Cheon, H. G.; Kim, J. H.; Min, B.-H.; Lee, H. B.; Kim, M. S. Small intestine submucosa sponge for in vivo support of tissue-engineered bone formation in the presence of rat bone marrow stem cells. *Biomaterials* **2010**, *31* (6), 1104–1113.

(38) Harada, N.; Watanabe, Y.; Sato, K.; Abe, S.; Yamanaka, K.; Sakai, Y.; Kaneko, T.; Matsushita, T. Bone regeneration in a massive rat femur defect through endochondral ossification achieved with chondrogenically differentiated MSCs in a degradable scaffold. *Biomaterials* **2014**, *35* (27), 7800–7810.

(39) Purohit, M. P.; Verma, N. K.; Kar, A. K.; Singh, A.; Ghosh, D.; Patnaik, S. Inhibition of thioredoxin reductase by targeted selenopolymeric nanocarriers synergizes the therapeutic efficacy of doxorubicin in MCF7 human breast cancer cells. *ACS Appl. Mater. Interfaces* **2017**, *9* (42), 36493–36512.

(40) Satija, N. K.; Sharma, D.; Afrin, F.; Tripathi, R. P.; Gangenahalli, G. High throughput transcriptome profiling of lithium stimulated human mesenchymal stem cells reveals priming towards osteoblastic lineage. *PLoS One* **2013**, *8* (1), e55769.

(41) Stein, G. S.; Lian, J. B.; Stein, J. L.; Van Wijnen, A. J.; Montecino, M. Transcriptional control of osteoblast growth and differentiation. *Physiol. Rev.* **1996**, *76* (2), 593–629.

(42) Tierney, C. M.; Haugh, M. G.; Liedl, J.; Mulcahy, F.; Hayes, B.; O'Brien, F. J. The effects of collagen concentration and crosslink density on the biological, structural and mechanical properties of collagen-GAG scaffolds for bone tissue engineering. *J. Mech. Behav. Biomed. Mater.* **2009**, *2* (2), 202–209.

(43) Verma, N. K.; Purohit, M. P.; Equbal, D.; Dhiman, N.; Singh, A.; Kar, A. K.; Shankar, J.; Tehlan, S.; Patnaik, S. Targeted smart pH and thermoresponsive N, O-carboxymethyl chitosan conjugated

nanogels for enhanced therapeutic efficacy of doxorubicin in MCF-7 breast cancer cells. *Bioconjugate Chem.* **2016**, *27* (11), 2605–2619.

(44) Ma, L.; Gao, C.; Mao, Z.; Zhou, J.; Shen, J.; Hu, X.; Han, C. Collagen/chitosan porous scaffolds with improved biostability for skin tissue engineering. *Biomaterials* **2003**, *24* (26), 4833–4841.

(45) Curcio, M.; Puoci, F.; Iemma, F.; Parisi, O. I.; Cirillo, G.; Spizzirri, U. G.; Picci, N. Covalent insertion of antioxidant molecules on chitosan by a free radical grafting procedure. *J. Agric. Food Chem.* **2009**, *57* (13), 5933–5938.

(46) Kar, A. K.; Singh, A.; Dhiman, N.; Purohit, M. P.; Jagdale, P.; Kamthan, M.; Singh, D.; Kumar, M.; Ghosh, D.; Patnaik, S. Polymer-Assisted In Situ Synthesis of Silver Nanoparticles with Epigallocatechin Gallate (EGCG) Impregnated Wound Patch Potentiate Controlled Inflammatory Responses for Brisk Wound Healing. *Int. J. Nanomed.* **2019**, *14*, 9837–9854.

(47) Xu, C.; Lee, W.; Dai, G.; Hong, Y. Highly elastic biodegradable single-network hydrogel for cell printing. *ACS Appl. Mater. Interfaces* **2018**, *10* (12), 9969–9979.

(48) Meinel, L.; Fajardo, R.; Hofmann, S.; Langer, R.; Chen, J.; Snyder, B.; Vunjak-Novakovic, G.; Kaplan, D. Silk implants for the healing of critical size bone defects. *Bone* **2005**, *37* (5), 688–698.

(49) Pal, S.; Khan, H.; China, S. P.; Mittal, M.; Porwal, K.; Shrivastava, R.; Taneja, I.; Hossain, Z.; Mandalapu, D.; Gayen, J. R.; Wahajuddin, M.; Sharma, V. L.; Trivedi, A. K.; Sanyal, S.; Bhadauria, S.; Godbole, M. M.; Gupta, S. K.; Chattopadhyay, N. Theophylline, a methylxanthine drug induces osteopenia and alters calcitropic hormones, and prophylactic vitamin D treatment protects against these changes in rats. *Toxicol. Appl. Pharmacol.* **2016**, *295*, 12–25.

(50) Yan, Y.; Chen, H.; Zhang, H.; Guo, C.; Yang, K.; Chen, K.; Cheng, R.; Qian, N.; Sandler, N.; Zhang, Y. S.; Shen, H.; Qi, J.; Cui, W.; Deng, L. Vascularized 3D printed scaffolds for promoting bone regeneration. *Biomaterials* **2019**, *190–191*, 97–110.

(51) Saita, Y.; Takagi, T.; Kitahara, K.; Usui, M.; Miyazono, K.; Ezura, Y.; Nakashima, K.; Kurosawa, H.; Ishii, S.; Noda, M. Lack of Schnurri-2 expression associates with reduced bone remodeling and osteopenia. *J. Biol. Chem.* **2007**, *282* (17), 12907–15.

(52) Soleimani, M.; Nadri, S. A protocol for isolation and culture of mesenchymal stem cells from mouse bone marrow. *Nat. Protoc.* **2009**, *4* (1), 102.

(53) Abreu, F. R. d.; Campana-Filho, S. P. Preparation and characterization of carboxymethylchitosan. *Polim.: Cienc. Tecnol.* **2005**, *15* (2), 79–83.

(54) Chen, S.-C.; Wu, Y.-C.; Mi, F.-L.; Lin, Y.-H.; Yu, L.-C.; Sung, H.-W. A novel pH-sensitive hydrogel composed of N,O-carboxymethyl chitosan and alginate cross-linked by genipin for protein drug delivery. *J. Controlled Release* **2004**, *96* (2), 285–300.

(55) Lei, F.; Wang, X.; Liang, C.; Yuan, F.; Gao, Y. Preparation and functional evaluation of chitosan-EGCG conjugates. *J. Appl. Polym. Sci.* **2014**, *131* (3), 39732.

(56) Masuda, M.; Karube, S.; Hayashi, Y.; Shindo, H.; Igarashi, M. Direct measurement of collagen crosslinks with automatic amino acid analyzer-identification of peaks due to crosslinks. *FEBS Lett.* **1976**, *63* (2), 245–249.

(57) Martínez, A.; Blanco, M. D.; Davidenko, N.; Cameron, R. E. Tailoring chitosan/collagen scaffolds for tissue engineering: Effect of composition and different crosslinking agents on scaffold properties. *Carbohydr. Polym.* **2015**, *132*, 606–19.

(58) Riaz, T.; Zeeshan, R.; Zarif, F.; Ilyas, K.; Muhammad, N.; Safi, S. Z.; Rahim, A.; Rizvi, S. A.; Rehman, I. U. FTIR analysis of natural and synthetic collagen. *Appl. Spectrosc. Rev.* **2018**, *53*, 703–746.

(59) Kim, J.-W.; Yang, B.-E.; Hong, S.-J.; Choi, H.-G.; Byeon, S.-J.; Lim, H.-K.; Chung, S.-M.; Lee, J.-H.; Byun, S.-H. Bone Regeneration Capability of 3D Printed Ceramic Scaffolds. *Int. J. Mol. Sci.* **2020**, *21* (14), 4837.

(60) Shih, Y.-R. V.; Liu, M.; Kwon, S. K.; Iida, M.; Gong, Y.; Sangaj, N.; Varghese, S. Dysregulation of ectonucleotidase-mediated extracellular adenosine during postmenopausal bone loss. *Sci. Adv.* **2019**, *5* (8), eaax1387.

(61) Cui, H.; Wang, Y.; Cui, L.; Zhang, P.; Wang, X.; Wei, Y.; Chen, X. In vitro studies on regulation of osteogenic activities by electrical stimulus on biodegradable electroactive polyelectrolyte multilayers. *Biomacromolecules* **2014**, *15* (8), 3146–3157.

(62) Jin, P.; Li, M.; Xu, G.; Zhang, K.; Zheng, L. I.; Zhao, J. Role of (–)-epigallocatechin-3-gallate in the osteogenic differentiation of human bone marrow mesenchymal stem cells: An enhancer or an inducer? *Exp. Ther. Med.* **2015**, *10* (2), 828–834.

(63) Cabrera, C.; Giménez, R.; López, M. C. Determination of tea components with antioxidant activity. *J. Agric. Food Chem.* **2003**, *51* (15), 4427–4435.

(64) Hu, X.; Neoh, K.-G.; Shi, Z.; Kang, E.-T.; Poh, C.; Wang, W. An in vitro assessment of titanium functionalized with polysaccharides conjugated with vascular endothelial growth factor for enhanced osseointegration and inhibition of bacterial adhesion. *Biomaterials* **2010**, *31* (34), 8854–8863.

(65) Levengood, S. K. L.; Zhang, M. Chitosan-based scaffolds for bone tissue engineering. *J. Mater. Chem. B* **2014**, *2* (21), 3161–3184.

(66) Heino, J. The collagen family members as cell adhesion proteins. *BioEssays* **2007**, *29* (10), 1001–1010.

(67) Salaszyk, R. M.; Williams, W. A.; Boskey, A.; Batorsky, A.; Plopper, G. E. Adhesion to vitronectin and collagen I promotes osteogenic differentiation of human mesenchymal stem cells. *J. Biomed. Biotechnol.* **2004**, *2004* (1), 24–34.

(68) Mathews, S.; Bhonde, R.; Gupta, P. K.; Totey, S. A novel tripolymer coating demonstrating the synergistic effect of chitosan, collagen type I and hyaluronic acid on osteogenic differentiation of human bone marrow derived mesenchymal stem cells. *Biochem. Biophys. Res. Commun.* **2011**, *414* (1), 270–276.

(69) Madhally, S. V.; Matthew, H. W. Porous chitosan scaffolds for tissue engineering. *Biomaterials* **1999**, *20* (12), 1133–1142.

(70) Chu, C.; Deng, J.; Xiang, L.; Wu, Y.; Wei, X.; Qu, Y.; Man, Y. Evaluation of epigallocatechin-3-gallate (EGCG) cross-linked collagen membranes and concerns on osteoblasts. *Mater. Sci. Eng., C* **2016**, *67*, 386–394.

(71) Lee, B. S.; Lee, C. C.; Lin, H. P.; Shih, W. A.; Hsieh, W. L.; Lai, C. H.; Takeuchi, Y.; Chen, Y. W. A functional chitosan membrane with grafted epigallocatechin-3-gallate and lovastatin enhances periodontal tissue regeneration in dogs. *Carbohydr. Polym.* **2016**, *151*, 790–802.

(72) Somaiah, C.; Kumar, A.; Mawrie, D.; Sharma, A.; Patil, S. D.; Bhattacharyya, J.; Swaminathan, R.; Jaganathan, B. G. Collagen promotes higher adhesion, survival and proliferation of mesenchymal stem cells. *PLoS One* **2015**, *10* (12), e0145068.

(73) Karageorgiou, V.; Kaplan, D. Porosity of 3D biomaterial scaffolds and osteogenesis. *Biomaterials* **2005**, *26* (27), 5474–5491.

(74) Rezwan, K.; Chen, Q.; Blaker, J.; Boccaccini, A. R. Biodegradable and bioactive porous polymer/inorganic composite scaffolds for bone tissue engineering. *Biomaterials* **2006**, *27* (18), 3413–3431.